Catalysis Science & Technology

ROYAL SOCIETY OF CHEMISTRY

PAPER

View Article Online
View Journal

Cite this: DOI: 10.1039/d6cy00219f

Impact of solvated hydronium ions and local pH on H_2O_2 direct synthesis over Pd catalysts supported on Brønsted acid solids

Tomas Ricciardulli,†[a] Sucharita Vijayaraghavan, †[b] Jason S. Adams[a] and David W. Flaherty*[b]

Supported Pd nanoparticles exhibit insufficient rates and selectivities for H_2O_2 direct synthesis (H_2 + O_2 → H_2O_2) in pure aqueous solvents, limiting cost-effective production. Water soluble mineral acids increase H_2O_2 formation rates and selectivities but corrode solid catalysts and process equipment. Here, we synthesize Pd catalysts supported on aluminosilicate zeolites (CHA, MFI, BEA, FAU), and other Brønsted acid materials (sulfonic acid resin, Al-MCM-41) and examine how acid properties and zeolite confinement influence H_2O_2 kinetics. Infrared spectra of adsorbed CO reveal Pd exists as both single atoms and nanoparticles. Comparisons of apparent activation enthalpies for H_2O_2 and H_2O formation demonstrate Pd nanoparticles contribute to observed rates, but ion-exchanged Pd atoms at Brønsted acid sites remain inactive. Pd supported on medium- and large-pore zeolites (BEA, FAU) give ~10-fold higher H_2O_2 rates than small-pore zeolites (MFI, CHA) and provide similar selectivities (60–70%). Other Brønsted acid supports yield H_2O_2 formation rates comparable to the zeolites, and all solid acid supports deliver greater H_2O_2 selectivities than SiO_2 and Al_2O_3, which suggests that zeolite topology alone does not account for kinetic differences. Combined assessment of rate measurements on physical mixtures and measured points of zero charge indicate that the greater H_2O_2 selectivities on Brønsted acid supports stems largely from decreases in the fluid-phase pH, where higher concentrations of H_3O^+ enthalpically destabilize transition states for H_2O_2 formation (by 5–10 kJ mol^{-1}) and more significantly impact H_2O formation (25–50 kJ mol^{-1}). These findings demonstrate that local pH influences apparent enthalpies for catalysis and offers an alternative to soluble acid promoters for H_2O_2 synthesis.

Received 21st February 2026,
Accepted 31st May 2026

DOI: 10.1039/d6cy00219f

rsc.li/catalysis

1. Introduction

The catalytic reduction of O_2 with H_2 to H_2O_2 promises a cost-effective alternative to the energy and capital-intensive anthraquinone auto-oxidation process.[1] Attaining high selectivities toward H_2O_2 remains a challenge, because catalysts active for H_2O_2 formation also promote decomposition and hydrogenation reactions that consume H_2O_2 and form H_2O.[2] Monometallic Pd and Pt catalysts typically exhibit high H_2 oxidation rates but low H_2O_2 selectivities (<40%), which motivates strategies to increase H_2O_2 selectivities of these catalysts without sacrificing the chemical purity or stability of the reactor effluent (*e.g.*, avoiding acid[3,4] and halide promoters[5–7] and organic solvents[8–10]). One successful approach involves creation of Pd- or Pt-bimetallics (*e.g.*, by alloying with Au), which leads to greater barriers for elementary steps that cleave O–O bonds compared to those for proton–electron transfer (PET) steps that oxidize H_2 and reduce O_2 to H_2O_2.[11,12] These kinetic differences lead to bimetallics[13–17] and single-atom alloy[11,12,18] catalysts that provide primary selectivities to H_2O_2 that exceed 95%. These selective alloy nanoparticle catalysts contain high mole fractions of the less reactive metal (*e.g.*, Au) and expose small fractions of the Pd- or Pt-atoms to reactants, which lead to high catalyst costs and low rates normalized by mass of precious metal.[19] Consequently, alternative strategies to improve selectivities without the drawbacks of alloying with costly metals remain necessary.

Methods to do so involve modifying the solvation environment around the surface of Pd nanoparticles by either adding co-adsorbates that bind to Pd surfaces or introducing changes to the pH and structure of aqueous water at the solid–liquid interface. Ligand-functionalized Pd nanoparticles, for example, show greater selectivities to H_2O_2, which the authors interpreted as evidence that oxygenated ligands preferentially stabilize key reaction intermediates (O_2^*, OOH*)

[a] *Department of Chemical and Biomolecular Engineering, University of Illinois Urbana-Champaign, Urbana, IL 61801, USA*
[b] *School of Chemical and Biomolecular Engineering, Georgia Institute of Technology, Atlanta, GA, 30032, USA. E-mail: dflaherty3@gatech.edu*
† Equal contribution.

associated with H_2O_2 formation over those that form water *via* hydrogen bonding.[20,21] These findings differ from conclusions of computational studies that suggest the hydrogen bonding effects on reaction thermodynamics impact reactants and products to a similar extent, and thus, lead to minimal changes.[22] Additionally, the water present in the aqueous solvent seems to be a more effective hydrogen bond donor and acceptor than organic ligands. Other explanations describe electrostatic stabilization of transition states or the formation of surface redox mediators both of which may influence barriers for PET processes.[10,22,23] The addition of mineral acids (*e.g.*, HCl, HNO_3, H_3PO_4, H_2SO_4) can increase selectivities substantially (increase from ~40% to more than 80%); however, the extent of improvement appears to rely on the presence of organic cosolvents, and the anionic complexes inhibit or corrode Pd nanoparticles over extended periods.[2,8,9,24] Nevertheless, these observations suggest that increases to the concentration of hydronium ions ($[H_3O^+]$, *i.e.*, decreases in pH) lead to significant changes in rates of key elementary steps.

Pd catalysts supported on Brønsted-acidic materials provide higher H_2O_2 selectivities, in ways reminiscent of soluble mineral acid promoters. These similarities may be rationalized by considering that Brønsted acid sites on solid materials dissociate and yield solvated protons in the presence of liquids (*e.g.*, $H^+(H_2O)_8$ in H_2O-containing H-MFI).[25] This suggests that solvated protons in water-containing zeolites, akin to H_3O^+, may contribute to the differences in rates and selectivities reported. Similar trends have been observed on other Brønsted acidic supports, such as heterogeneous polyoxometallates,[3,26–28] sulfated zirconia,[29–31] and sulfonic acid-functionalized materials,[32–35] although most publications attribute catalytic differences to a modification in the oxidation states of Pd rather than local solvation effects. Confinement of the metal nanoparticles within zeolites also appears to impact catalytic outcomes. PdAu nanoparticles confined within the pores of ZSM-5 zeolites exhibit a large increase in H_2O_2 rates and selectivities (38% to 90%) compared to PdAu nanoparticles on the external surface.[36] Similarly, Pd nanoparticles stabilized in SnO_x-containing MFI zeolites provide greater H_2O_2 formation rates.[37] Possible explanations for the improved catalytic performance in these systems include changes to the organization of solvating molecules introduced by Brønsted acid sites, modifications to free energy landscapes arising from electron redistribution caused by charge-transfer interactions,[38–41] and the emergence of local electric fields that influence the stabilities of adsorbates and transition states.[42–44] Similar phenomena impact rates for hydrogen oxidation,[45,46] oxygen reduction,[15,47,48] and epoxidation reactions.[39]

Here, we describe the identity of active sites, the role of local H_3O^+ concentration, and the impact of confined solvent structures on direct synthesis of H_2O_2 by creating, characterizing, and catalytically interrogating a series of catalysts comprised of Pd nanoparticles upon distinct forms of Brønsted acidic supports. Notably, reported rates do not suffer from transport artifacts frequently encountered during liquid-phase conversions on zeolite catalysts. Steady-state turnover rates and selectivities for H_2O_2 formation over Pd nanoparticles present within a series of solid Brønsted acids (aluminosilicate zeolites, mesoporous aluminosilicates, and sulfonic acid polymer resins) consistently exceed those measured upon Pd–SiO_2 and Pd–Al_2O_3 materials. Formation of aggregates that combine the Brønsted acid form of FAU (H-FAU) with either Pd–SiO_2 and Pd–Al_2O_3 decreases the solution phase pH and modestly increases the H_2O_2 selectivity, which implies the local concentrations of H_3O^+ impact rates of selected steps. Notably, the catalyst consisting of Pd nanoparticles within FAU (Pd-FAU) gives the greatest H_2O_2 selectivities (72%) and turnover rates (0.22 $mol_{H_2O_2}$ mol_{Pd}^{-1} s^{-1}) under reaction conditions. Correlations between *ex situ* infrared spectra of adsorbed CO and catalytic rates and selectivities across a series of Pd-FAU catalysts with distinct Pd contents show that Pd nanoparticles and single atoms coexist in acidic FAU pores, but only nanoparticles contribute to observed rates. Comparisons among apparent activation enthalpies for the oxidation of H_2 and the formation of H_2O_2 and H_2O across a series of eight distinct catalysts with variations in topology, Brønsted acid character, and physical proximity between acid sites and Pd nanoparticles indicate that high local concentrations of H_3O^+ preferentially destabilize transition states that activate H_2 and form H_2O, yet only modestly impact those for H_2O_2 production. These trends emerge most clearly when atomic hydrogen saturates Pd active sites and attenuate significantly when O_2-derived species cover the catalyst surface. These observations suggest that solvated H_3O^+ promotes H_2O_2 synthesis through outer-sphere interactions between adsorbate and solvent molecules.

2. Materials and methods

2.1. Synthesis of supported Pd catalysts

Pd was incorporated into commercially available H^+ or NH_4^+ form zeolites and aluminosilicates using ion-exchange and oxidative dispersion methods described by Sachtler.[49] A slurry (4 g, 200 cm^3, 50 cm^3 g^{-1}) of zeolite in deionized water (Brønsted, >17.8 MΩ cm^{-1}) was prepared under 500 rpm stirring by a magnetic stir bar, and 0.89 cm^3 of a 8.4 mM solution of Pd $(NH_3)_4Cl_2$ (Sigma-Aldrich, >99.99% trace metals basis) was added dropwise. This solution was agitated overnight, centrifuged (5000 rpm, 30 minutes), and dried under ambient conditions for at least 72 hours. During the drying process, the centrifuge tubes were covered with KimWipes to protect the catalyst from contamination. The dried catalysts were loaded into catalyst boats which were then placed into a tube furnace and thermally calcined (1 K min^{-1}, 823 K, 4 h) under a mixture of flowing dry air (25 cm^3 min^{-1} g^{-1}) and He (50 cm^3 min^{-1} g^{-1}). Most catalysts were subsequently reduced under variable temperatures (20 kPa H_2, 81 kPa He, 200 cm^3 min^{-1}, 1 K min^{-1}, 473–773 K, 2 h) to investigate the impact on catalysis.

Pd was supported on conventional SiO_2 (Davisil 646, Sigma-Aldrich) and γ-Al_2O_3 (Al_2O_3; Catalox, HP 14/150 Alumina) supports using strong electrostatic adsorption techniques. A solution of NH_4OH (100 cm^3, Macron, 28–30%) and deionized H_2O (200 cm^3) was added to 6 g of Al_2O_3 and stirred. A solution of aqueous 3.9 mM $Pd(NH_3)_4Cl_2$ (7.22 cm^3) was added dropwise and the mixture was stirred for 24 hours. The mixtures were centrifuged (5000 rpm, 30 minutes) to extract the Pd–Al_2O_3 catalyst, which was redispersed in 400 cm^3 deionized H_2O and centrifuged again. The supernatant was decanted, and the solids were dried under ambient conditions for 72 h and thermally reduced (20 kPa H_2, 81 kPa He, 200 cm^3 min^{-1}) in a tube furnace (573 K, 2 h, 3 K min^{-1}).

Sulfonic acid resins decompose upon exposure to temperatures hot enough for H_2 to reduce supported Pd cations. Consequently, a different synthesis method was used to prepare the Pd supported on sulfonic acid resin. A quantity (5.3 g) of a sulfonic acid resin (DOWEX 50WX8 hydrogen form, Sigma-Aldrich) was added to methanol (20 cm^3). While stirring the resin mixture, 5 cm^3 of a freshly prepared 10.7 mM aqueous $Pd(NO_3)_2$ (Sigma-Aldrich, ~40% Pd) solution was added in a dropwise manner. The mixture was allowed to dry under ambient conditions, then the solids were collected, vacuum filtered and washed with deionized water (400 cm^3) to remove loosely bound Pd species. Table 1 shows the Si/Al ratio, Pd weight loading measured by ICP-OES, surface-averaged mean diameter of Pd nanoparticles post reduction at 773 K (Section S1), Pd dispersion measured using CO chemisorption (Section S2), and the point of zero charge of the support (Section S3).

2.2. Determination of the point of zero charge of oxide supports

The point of zero charge (PZC) of the catalyst support materials was measured using a technique previously reported by Noh and Schwarz.[50] Aliquots (2.5 cm^3) of degassed deionized H_2O (pH 7) were incrementally added to 500 mg of the solid sample. The slurry was continuously sparged with flowing He, and equilibrium values of the pH were measured (Oakton, pH 450) as a function of the slurry concentration. The point of zero charge was calculated by extrapolating measurements of the pH as a function of solution volume to a volume that matched the pore volume of the support (Section S3).[51]

2.3. Measurement of steady-state H_2O_2 and H_2O formation rates

Rates of H_2O_2 and H_2O formation were measured using a steady-state packed-bed plug-flow reactor system detailed in previous reports.[10–12,52] The zeolitic catalysts were mixed with equal parts γ-Al_2O_3 (Al_2O_3; Catalox, HP 14/150 alumina) by weight as a binder, pelletized (140 MPa, 30 minutes) in a laboratory pellet press (Carver, model C), crushed and sieved to yield 250 to 500 micron diameter aggregates (35–60 mesh). Mixing with Al_2O_3 did not significantly impact the catalyst performance but helped to prevent catalyst pellet attrition during testing. Each catalyst (200 mg, 35–60 mesh) was physically mixed with a silica diluent (800 mg SiO_2, Davisil 646, 35–60 mesh). The physical mixture was transferred into a stainless-steel tube (1 cm inner diameter), in which the catalyst bed was mechanically supported using a combination of glass wool (Sigma Aldrich, silanized), glass rods, and fritted nickel gaskets.

Reactions were conducted with continuous flow of water and the gaseous reactants. Deionized H_2O (>17.8 MΩ cm^{-1}) was degassed with Ar and pumped through the system using an HPLC pump (SSI, M1-Class) at constant liquid flowrate (35 cm^3 min^{-1}). The liquid contacted and mixed with a flowing gas stream that contained H_2, O_2 and N_2 with a composition and total flowrate (50–100 cm^3 min^{-1}) set by mass flow controllers (Parker-Porter) connected to high-pressure gas cylinders (25% H_2 balance N_2 and 5% O_2 balance N_2, Airgas,

Table 1 List of Pd catalysts on different supports used in this study with Si/Al ratio, bulk Pd weight loading, surface-averaged mean diameter of Pd nanoparticles measured by TEM, Pd nanoparticle diameter estimated from CO chemisorption, and the point of zero charge (PZC) of the respective support

Catalyst	Si/Al[a]	Pd loading[b] (wt%)	$<d_{TEM}>^c$ (nm)	$<d_{CHEM}>^d$ (nm)	Support PZC
Pd-FAU	6	0.02	3.2 ± 0.8	1.1	4.0 ± 0.2
Pd-FAU	15	0.02	2.4 ± 0.6	2.0	3.8 ± 0.2
Pd-FAU	40	0.02	2.2 ± 0.5	1.8	3.5 ± 0.4
Pd-FAU	385	0.02	3.5 ± 0.9	1.7	3.9 ± 0.4
Pd-BEA	14	0.02	5.8 ± 1.8	1.1	3.2 ± 0.4
Pd-MFI	11.5	0.02	3.1 ± 0.9	1.4	3.2 ± 0.2
Pd-CHA	30	0.02	2.2 ± 0.5	1.3	3.7 ± 0.2
Pd-Al-MCM-41	10	0.02	5.7 ± 2.0	1.8	5.1 ± 0.6
Pd-γ-Al_2O_3	n/a	0.03	4.7 ± 1.4	2.9	6.7 ± 0.1
Pd–SiO_2	n/a	0.05	3.4 ± 1.0	1.2	6.9 ± 0.1[g]
Pd-DOWEX	n/a	0.05	16.1 ± 4.5[e]	12.9[f]	2.3 ± 0.6

[a] Manufacturer specification. [b] Measured by ICP-OES. [c] Surface-averaged diameter measured by TEM after reduction at 773 K (Fig. S1). [d] Nanoparticle diameter from Pd dispersion measured by CO chemisorption after *in situ* reduction at 573 K on samples reduced *ex situ* at 773 K (Section S2). [e] No thermal pretreatment, dried at ambient temperature – prone to decomposing over time. [f] Pd dispersion measured after *in situ* reduction at 373 K. [g] Consistent agreement with manufacturer specifications.

99.999%). The mixed gas–liquid stream then entered the packed-bed reactor where the reactor pressure was set by a back-pressure regulator (Equilibar, EB1LF1-SS316) controlled by an electronic pressure reducer (Proportion Air, QB1S). The temperature was maintained by continuously flowing refrigerant (50 v% aqueous ethylene glycol) from a recirculating bath (Fisher Scientific, Isotemp) to the jacketed reactor body while measuring temperature with a K-type thermocouple embedded in the reactor jacket. The reactor effluent was divided into gas and liquid streams using a simple gas–liquid separator controlled with an electronically actuated valve (Banjo LEV025PL).

Reactant consumption and product formation rates were determined by compositional analysis of the gas and liquid effluent. The H_2 conversion was monitored using a gas chromatograph (Agilent 7890) with a thermal conductivity detector using Ar as a carrier and reference gas. An electronically controlled 10-port valve (Vici) was used to deliver equal volumes (1.0 cm^3) of sample and a colorimetric indicator (4.1 mM $CuSO_4$, VWR, ≥98%; 6.0 mM neocuproine, SageChem, ≥98%; 25% v/v Ethanol/H_2O) to an automated fraction collector (BioRad 2110) loaded with test tubes (Fisherbrand, 13 × 100 mm). The H_2O_2 concentration was determined using UV-vis spectroscopy (Spectronic 20 Genesys) to measure absorbance at 454 nm in conjunction with calibration curves obtained using solutions of known H_2O_2 concentration. The H_2O formation rates are calculated as the difference between the H_2 consumption and H_2O_2 formation rates. The impact of transport restrictions on catalysis were are assessed by verification of the Madon–Boudart criterion[53] using Pd–FAU catalysts with variable Pd loading reduced *ex situ* at 473 K (SI Section S4). From these data, rate measurements were confirmed to be obtained in the absence of internal and external mass transfer limitations for all zeolite-supported Pd nanoparticles. Reported steady-state kinetics were measured under differential conversion of H_2 (2–5%), which results in extremely low concentrations of H_2O_2, minimizes the impact of secondary reactions of H_2O_2, and allows measurement of intrinsic kinetics and primary product formation rates.

The rates and reversibility of hydrogen activation were assessed using reactant mixtures of H_2 and D_2 together with O_2. Formation rates of HD during H_2O_2 synthesis catalysis were measured using mass spectrometry (Pfeiffer, ThermoStar) while cofeeding equimolar flowrates (*i.e.*, equal partial pressures) of H_2 and D_2 in the presence of a constant amount of oxygen (60 kPa O_2) in flowing H_2O.

2.4. Vibrational transmission spectroscopy of adsorbed CO

Infrared spectra of carbon monoxide (CO*) bound to Pd catalysts were measured using a Fourier transform infrared (FTIR) spectrometer (Bruker, Tensor 37) equipped with a HgCdTe detector cooled by liquid N_2. Catalyst samples were crushed into a fine powder and pressed into self-supporting disks using a pellet press (Carver, Model C). The catalysts disks were then loaded into a transmission infrared cell described previously.[54] The catalyst was mounted in between two stainless steel retaining rings, and the cell was sealed by compressing a graphite ferrule (Chromalytic Technology Pty. Ltd.) against a stainless steel ferrule and CaF_2 windows. The cell was mounted into the sample compartment of the spectrometer, connected to a gas manifold and checked for leaks. Gases (He, H_2, O_2, 1% CO in He, Airgas, 99.999%) were introduced to the cell through mass flow controllers (Alicat, MC Series) connected to the gas manifold. The cell temperature was set using a PID controller (Watlow) with resistive heaters (Omega). Prior to measurement, catalysts were pretreated from 423–773 K oxidizing (20 kPa O_2, 81 kPa He, 30 cm^3 min^{-1}), reducing (20 kPa H_2, 81 kPa He, 30 cm^3 min^{-1}) or inert (101 kPa He, 30 cm^3 min^{-1}) atmospheres, held for 2 h, and then cooled to 303 K in flowing He (101 kPa He, 24 cm^3 min^{-1}). Once the sample stabilized at 303 K, a background scan was taken (1 cm^{-1} resolution, zero-filling factor of 2, 128 scans coadded), the flow was switched to dilute CO (0.1 kPa CO, 100.9 kPa He, 20 cm^3 min^{-1}) and sample spectra were taken (1 cm^{-1}, 32 scans averaged for each spectrum) until the system achieved steady-state, which typically required 20 minutes.

3. Results and discussion

3.1. Influence of catalyst support identity on H_2O_2 formation rates and selectivities

Fig. 1 shows that primary product formation rates and selectivities for the catalytic reactions among O_2 and H_2 depend on the identity of the support material and appear sensitive to the pore structure and presence of Brønsted acid

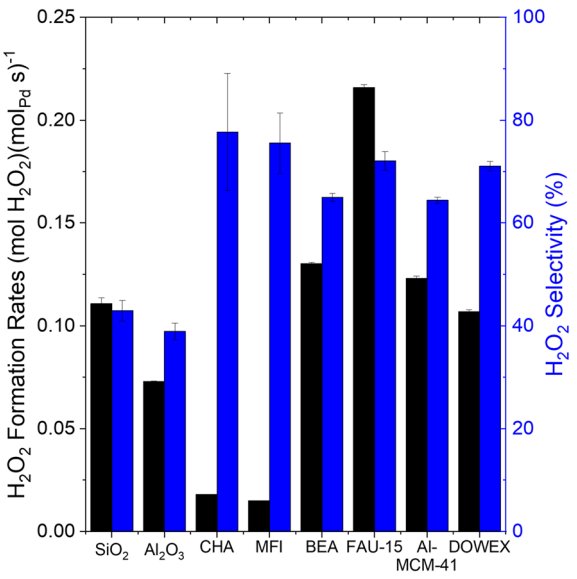

Fig. 1 H_2O_2 formation rates (black) and selectivities (blue) for Pd catalysts on different supports at standard reaction conditions (200 kPa H_2, 60 kPa O_2, 286 K).

functions of the support. Among microporous aluminosilicates, catalysts formed from small pore zeolites (CHA, MFI) give the lowest H_2O_2 formation rates (normalized by total quantity of Pd; ~0.016 mol H_2O_2 mol Pd^{-1} s^{-1}), and rates in larger pore zeolites (BEA, FAU) reach values more than 10-fold larger. Yet selectivities toward H_2O_2 remain similar among these zeolitic samples. Notably, measured formation rates for all these materials reflect intrinsic kinetics and not the influence of internal or external mass transfer limitations (*e.g.*, intraparticle concentration gradients, see SI Section S4).[55] Further, selectivities towards H_2O_2 remain similar across all Brønsted acid supports including zeolites, mesoporous aluminosilicate (Al-MCM-41), and sulfonic acid functionalized resin (DOWEX), but exceed those for Pd on SiO_2 or Al_2O_3 supports by nearly a factor of two.

These differences in rates and selectivities among different supports may reflect one or more structural distinctions within this series of materials. First, Pd nanoparticle size and dispersion measured from CO chemisorption and TEM indicate clear differences in nanoparticle structure and distribution of accessible active sites among the materials examined (Table 1): dispersions vary by a factor of 2–3 across the series of materials which correspond to mean particle diameters that range from 1.1 nm to 2.9 nm (comparisons exclude the resin supported Pd-DOWEX material). Further, nanoparticle diameters assessed by TEM appear systematically larger than mean diameters estimated from CO chemisorption for all samples, which implies the inability to detect a significant fraction of subnanometer Pd clusters on these supports.

Turnover rates normalized by accessible surface Pd calculated by CO chemisorption (Fig. S6) and TEM (Fig. S7) result in no systematic trends, suggesting that the nanoparticle size or variations in the quantity of accessible Pd across the range of materials examined here do not significantly govern catalyst reactivity. Second, rates of H_2O_2 formation depend on the void dimensions and topology of the microporous support for the Pd nanoparticles (Fig. S8). The zeolite with the largest internal voids (FAU, 1.2 nm supercages) shows the greatest H_2O_2 formation rates per total Pd, followed by medium pore zeolite (BEA, 0.6 nm) that gives rates ~10-fold higher than smaller pore zeolites (MFI and CHA, 0.5 and 0.4 nm, respectively). This trend suggests that confinement in smaller pore zeolites either alters the effective number of active sites, imposes diffusional limitations that hinder H_2O_2 formation, or modifies aspects of the solvent environment (*i.e.* amount and structure of confined water molecules) in ways that influence reactivity. Experiments to test the Madon–Boudart criterion for diffusion limitations (Section S4) confirm the absence of any diffusion constraints.

Studies on nanoconfined water, including recent *ab initio* and spectroscopic studies, show that small-pore zeolites like CHA and MFI impose strong ordering and reduce hydrogen-bonded networks, creating low-dimensional water clusters distinct from the extended, bulk-like clusters in larger-pore frameworks like FAU.[56,57] These confinement-induced structural changes occur even at fixed proton loading and are therefore distinct from purely thermodynamic shifts in local H_3O^+ concentration. At high water contents, the equilibrium proton activity is governed primarily by the framework's point of zero charge (PZC), while confinement plays a minor role in acidity.[58] Therefore, while PZC determines the local proton chemical potential experienced by Pd sites, the pore topology independently influences the structure, connectivity, and solvation environment of confined water molecules.[59] The increase in H_2O_2 formation rates with internal void diameter from CHA to FAU (Fig. 1) likely results from active site confinement within the pores and combined changes to the local H_3O^+ concentration, Pd solvation, stabilization of intermediates, and the proximity of Pd to Brønsted acid sites and structured water clusters, which all vary systematically with zeolite pore size or topology. In contrast, mesoporous materials (Al-MCM-41 and DOWEX) exhibit H_2O_2 formation rates more comparable to oxide supports (SiO_2 and Al_2O_3), and substantially lower rates than large-pore zeolites, possibly because these materials lack the beneficial confinement effects present in zeolitic frameworks.

While rates appear to differ with support topology, H_2O_2 selectivities remain similar across Brønsted acidic supports with small (CHA, MFI), medium (BEA), and large (FAU, MCM-41, DOWEX) voids (Fig. S8), which indicates that selectivities more strongly reflect other properties of the support material. Selectivities do not appear to depend on the differences in Pd nanoparticle size and dispersion estimated from CO chemisorption across these materials (Fig. S9 and S10). For instance, Pd supported on FAU contains predominantly 2 nm nanoparticles, yet exhibits higher rates and selectivities than the Pd nanoparticles supported on SiO_2 which are smaller (1.2 nm), as well as on Al_2O_3, which has larger Pd nanoparticles (2.9 nm). Moreover, despite substantial differences in nanoparticle sizes and Pd dispersion estimated from CO chemisorption among the various Brønsted acidic materials, they show similar H_2O_2 selectivities (Fig. 1). Previous reports on Pd particle size effects in H_2O_2 direct synthesis show varied trends in rates and selectivity that depend on support type, synthesis method, and reaction conditions. Most studies in semi-batch reactors use dilute ethanol, methanol, and sulfuric acid media with promoters under O_2-rich conditions and show that Pd nanoparticles larger than 2.5–3 nm exhibit lower H_2O_2 selectivity and rates due to increased Pd(111) facets that dissociate O_2 into water.[60–62] Wilson *et al.* demonstrated that in continuous flow reactors with dilute methanol, H_2O_2 selectivity and rates increase with Pd nanoparticle size (0.7 to 7 nm) under H_2- and O_2-rich conditions due to changes in the fraction of undercoordinated sites.[4] However, in purely aqueous media without promoters, smaller Pd nanoparticles (1.8 *versus* 11.8 nm) double H_2O_2 selectivity and increase H_2O_2 formation

rates tenfold due to changes in Pd dispersion and electronic effects that impact adsorbate binding.[63] Considering these previous reports on the influence of Pd nanoparticle size on H_2O_2 rates and selectivity,[4,52,56–59] the results presented in Fig. 1 and S9 and S10 indicate that Pd nanoparticle size and dispersion are not the dominant factors governing the observed H_2O_2 selectivity trends since the average diameters of Pd only vary between 1 and 3 nm.

Fig. 1 demonstrates that Brønsted acidic supports (aluminosilicate zeolites, Al-MCM-41, DOWEX) provide H_2O_2 selectivities in the range of 60–70%, which represents a two-fold increase over values for Pd on conventional support materials (*e.g.*, SiO_2, Al_2O_3). Contact between these materials and liquid water leads to pH values for the catalyst-liquid slurry that depend on the solid acid site density and the quantity of both solid and liquid in the slurry.[51] Table 1 presents measured values for the point of zero charge (PZC, or the isoelectronic point) obtained from measurements of the solution-phase pH values, which include contributions from both Brønsted (M–OH → M–O– + H^+) and Lewis acid sites ($M^+ + H_2O$ → M–OH + H^+). Aluminosilicates including zeolites and sulfonic acid resins present much lower PZC values (PZC = 2–4) than SiO_2 or Al_2O_3 (PZC ~ 7), and these materials also provide the greatest H_2O_2 selectivities (Fig. S11). This correlation suggests that selectivity differences among Pd nanoparticles on distinct supports result primarily from variations in surface charge among the aluminosilicate materials, solution pH, and Brønsted and Lewis acid strength, whereas H_2O_2 rates also depend on differences in support topology.

3.2. Active forms of Pd within zeolite catalysts

The size and nuclearity of Pd within the pores of microporous materials may influence rates and selectivities for H_2O_2 formation. For example, isolated Pd atoms on conductive supports exhibit high current densities and selectivities toward H_2O_2 formation by the two-electron reduction pathway during the electrocatalytic oxygen reduction reaction (*i.e.*, at cathodic potentials).[64,65] Bimetallic and single atom alloy nanoparticles (PdAu, PtAu, *etc.*) present high selectivities towards H_2O_2 during the direct synthesis reaction when Pd–Pd or Pt–Pt coordination numbers decrease due to dilution in Au matrices.[11,12] Atomically dispersed Pd species (*e.g.*, Pd^{2+}) form during oxidative treatments of Pd precursors and nanoparticles within aluminosilicate zeolites, because the electrostatic interactions of these cations stabilize anionic moieties within the zeolite framework.[49,66,67] Collectively, these prior observations present the possibility that isolated Pd cations may reside within microporous aluminosilicates and give rise to the systematically higher selectivities for H_2O_2 formation. Alternatively, these reactivity patterns may reflect contributions from Pd nanoparticles in contact with high local concentrations of H_3O^+ in pores or on the external surface of the zeolite particles. The fraction of Pd atoms that exist in either of these forms (*i.e.*, isolated cations or nanoparticles) depends on the thermal history of the catalyst, the composition of the support (*e.g.*, silicon to aluminum ratio, or number of sulfonic acid moieties), the quantity of palladium on the material, and the reaction conditions.[49,66,67] For example, oxidative treatments at elevated temperatures (*e.g.*, 823 K) or oxygen-rich reaction conditions disperse Pd nanoparticles into isolated cations stabilized by electrostatic interactions with Brønsted acid sites in zeolites.[66]

Fig. 2a compares steady-state H_2O_2 formation rates and selectivity for a series of Pd-FAU-15 catalysts created by distinct *ex situ* pretreatments selected with the intent to modify the fractions of Pd atoms that exist as isolated Pd cations or Pd nanoparticles on FAU (200 kPa H_2, 60 kPa O_2,

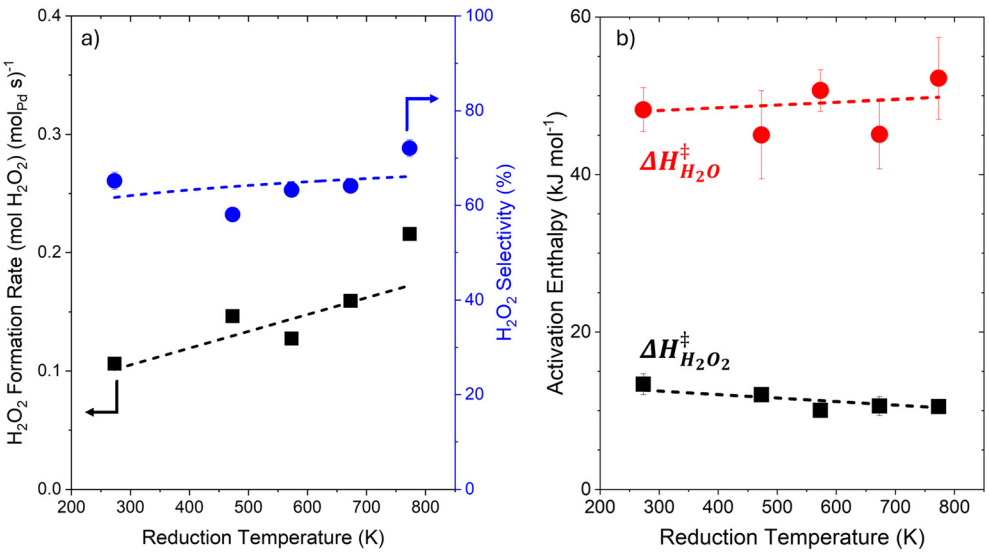

Fig. 2 (a) H_2O_2 formation rates (black ■) and selectivities (blue ●; 200 kPa H_2, 60 kPa O_2, 286 K), and (b) apparent activation enthalpies for H_2O_2 (black ■) and H_2O (red ●) formation (200 kPa H_2, 60 kPa O_2, 276–296 K) as functions of reduction temperature for 0.02 wt% Pd-FAU-15.

286 K). The catalyst reduced *ex situ* at 773 K achieves the highest H_2O_2 formation rates, while the catalyst reduced at 286 K (oxidized *ex situ* and reduced *in situ*) results in nearly two-fold lower rates. Despite the span of these H_2O_2 formation rates, the H_2O_2 selectivities vary non-monotonically and remain relatively similar (60–70%) for all reduction temperatures. Together, these observations suggest that the form of active sites primarily responsible for H_2O_2 formation (and H_2O formation) do not vary significantly between materials reduced at low and high temperatures. Fig. 2b shows that apparent activation enthalpies for H_2O_2 ($\Delta H^{\ddagger}_{H_2O_2}$ = 12 ± 2 kJ mol^{-1}) and H_2O ($\Delta H^{\ddagger}_{H_2O}$ = 45 ± 5 kJ mol^{-1}) formation change only slightly across the same series of Pd-FAU-15 catalysts (200 kPa H_2, 60 kPa O_2, 276–296 K; Fig. S12 and S13 present the measurements of rates as functions of inverse temperatures). Taken together, the minor differences in the values of H_2O_2 selectivities, $\Delta H^{\ddagger}_{H_2O_2}$, and $\Delta H^{\ddagger}_{H_2O}$ give evidence that higher temperature reductive treatments marginally alter the inherent reactivity of the active sites and increase the number of active sites considerably leading to higher H_2O_2 rates.

Infrared spectroscopy of adsorbed carbon monoxide (CO*) provides an opportunity to characterize the differences in the identity and relative populations of distinct Pd species (*i.e.*, isolated cations and nanoparticles) among the series of Pd-FAU-15 catalysts represented in Fig. 2. Fig. 3a shows vibrational spectra of CO* on Pd-FAU-15 following an *ex situ* oxidative (20 kPa O_2, 823 K, 2 h) treatment and a sequence of reductive treatments first in CO at 303 K (0.1 kPa CO, 303 K, 0.5 h), followed by treatments in hydrogen at increasing temperatures (20 kPa H_2, 473–773 K, 2 h) before CO exposure at 303 K again. The Pd-FAU-15 sample reduced under CO exposure at 303 K following the initial oxidative treatment yields weak vibrational features, which suggests a large fraction of Pd present does not bind CO. This observation suggests that most Pd atoms exist as isolated cations bound to the FAU support, because such sites weakly bind CO*.[49,67–71] Reduction at 473 K leads to the emergence of strong vibrational features at 2145 and 2125 cm^{-1}, which correspond to CO bound atop (η^1-CO*) to isolated Pd single atoms and Pd in small clusters, respectively. Furthermore, faint new broad features below 2000 cm^{-1} start to appear, which correspond to CO* at bridge (μ^2-CO*) configurations.[72–79] These features suggest the formation of small Pd nanoparticles or nanoclusters with reduction of the sample at elevated temperatures. Subsequent reductive treatments at higher temperatures (573–773 K) dampens the feature at 2145 cm^{-1} corresponding to CO* atop Pd single atoms. Increasing reduction temperature also leads to the broadening of the CO* atop Pd feature at 2125 cm^{-1} followed by a red-shift to 2110 cm^{-1}, and an increase in the bridge features (μ^2-CO*) suggesting the formation of larger nanoparticles with increasing temperatures.[80,81] The trends observed in these spectra give clear evidence for differences in the speciation of Pd atoms from isolated cations to reduced nanoparticles across the range of reductive treatments used.

Fig. 3b shows integrated peak areas for each of the three η^1-CO* features and the single μ^2-CO* feature observed in vibrational spectra (Fig. 3a) as functions of the temperature for the reductive treatment, which provides an indirect quantification of the relative abundance of isolated cationic Pd atoms and Pd nanoparticles available to bind CO. Contacting Pd-FAU only with CO at 303 K yields minimal

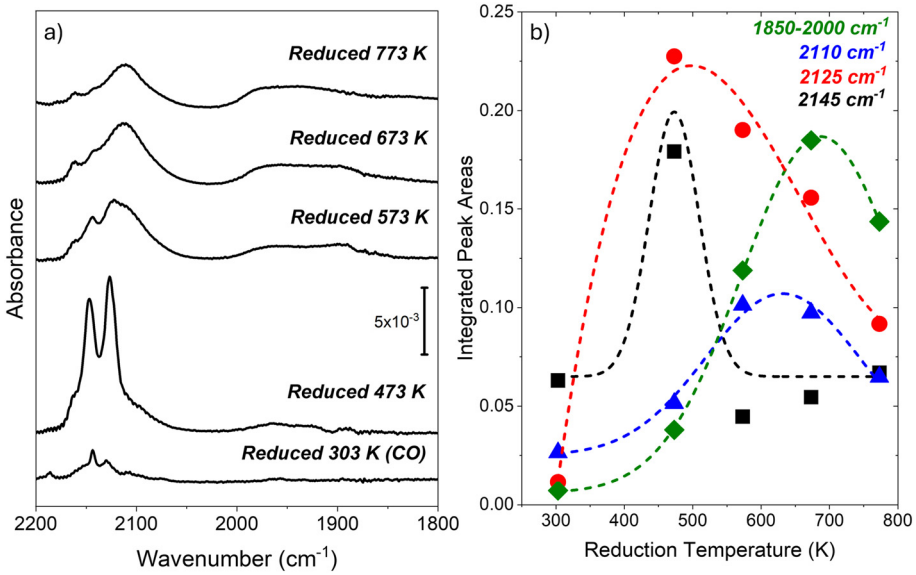

Fig. 3 (a) Infrared spectra of adsorbed CO on Pd-FAU-15 (0.1 kPa CO, 303 K) following sequential thermal treatments beginning with an *ex situ* oxidative treatment (20 kPa O_2) at 823 K followed directly by CO exposure (0.1 kPa CO, 303 K) followed by reductive treatments at temperatures indicated (20 kPa H_2). (b) Integrated peak areas for the η^1-CO* features at 2145 cm^{-1} (black ■), 2125 cm^{-1} (red ●), and 2110 cm^{-1} (blue ▲) and bridging CO peaks from 1850–2000 cm^{-1} (green ◆) shown as functions of the temperature for the reductive treatment. Dashed lines intended to guide the eyes.

peak area with intensity near 2145 cm^{-1}. The peaks corresponding to isolated cationic Pd atoms (2145 and 2125 cm^{-1}) achieve maximal intensity following reduction at 473 K in H_2, and these features attenuate with subsequent reductive treatments at higher temperatures (573–773 K). The area of the peak at 2110 cm^{-1} (CO atop Pd nanoparticles) increases with reductive treatment up to 573 K and decreases at higher temperatures. The area of the bridging CO peak (1850–2000 cm^{-1}) increases and reaches a maximum value at 673 K before declining. Both features associated with CO* on Pd nanoparticles decrease at reduction temperatures greater than 773 K. These trends demonstrate that isolated Pd cations reduce and coalesce at temperatures greater than 473 K to form Pd nanoparticles. The decrease in integrated peak areas of the Pd features observed at the highest reduction temperature may reflect reduced adsorbate coverages due to differences in CO binding strength or configuration on Pd as the speciation of Pd changes, rather than a decrease in the number of catalytically active Pd sites.[63] These observations together with the dependence of rates, selectivities, and apparent activation enthalpies on the reduction temperature for the Pd-FAU-15 catalysts (Fig. 2) give strong evidence that H_2O_2 and H_2O form by reactions that proceed on metallic Pd nanoparticles as opposed to isolated Pd cations.[10,82,83] Further, this interpretation contradicts recent reports that these reactions occur on isolated Pd cations in zeolitic materials.[36,84] The requirement for a metallic Pd nanoparticle becomes evident through an examination of the reaction mechanism.

3.3. Elementary steps and rate expressions for reactions among H_2 and O_2

Scheme 1 shows a system of elementary steps that account for formation of H_2O_2 and H_2O by reactions of O_2 and H_2 over metal nanoparticle catalysts that include Pd and Pd-based alloys.[6,10–12,23] This mechanism invokes two distinct types of sites ($^{\#}$ and *) to explain rates that lack an inhibitory effect of increasing H_2 or O_2 pressures along with other experimental and computational observations.

$$H_2 + 2^{\#} \rightleftharpoons 2H^{\#} \quad (1)$$
$$O_2 + * \rightleftharpoons O_2* \quad (2)$$
$$O_2* + H^{\#} + H_2O \longrightarrow OOH* + H_2O + {}^{\#} \quad (3)$$
$$OOH* + H^{\#} + H_2O \longrightarrow H_2O_2* + H_2O + {}^{\#} \quad (4)$$
$$OOH* + H^{\#} + H_2O \longrightarrow O* + 2H_2O + {}^{\#} \quad (5)$$
$$O* + H^{\#} + H_2O \longrightarrow OH* + H_2O + {}^{\#} \quad (6)$$
$$OH* + H^{\#} + H_2O \longrightarrow H_2O* + H_2O + {}^{\#} \quad (7)$$
$$H_2O_2* + H^{\#} + H_2O \longrightarrow OH* + 2H_2O + {}^{\#} \quad (8)$$
$$H_2O_2 + * \rightleftharpoons H_2O_2* \quad (9)$$
$$H_2O + * \rightleftharpoons H_2O* \quad (10)$$

Scheme 1 Proposed system of elementary steps describing H_2O_2 and H_2O formation on metal catalysts. The symbol → denotes an irreversible reaction, whereas ⇄ signifies a reversible reaction and ⇌ corresponds to a quasi-equilibrated reaction.

Hydrogen dissociatively adsorbs onto $^{\#}$ sites (step 1) and O_2 adsorbs molecularly on * sites (step 2). H_2O facilitates proton transfer in the rate-determining step (step 3), forming OOH* from reducing O_2^*. Both products (*i.e.*, H_2O_2 and H_2O) form by proton electron transfer to OOH* through selectivity determining steps (steps 4 and 5). Subsequent kinetically irrelevant processes (steps 6–10) remove oxygen- and hydrogen-derived intermediates from the surface to recover unoccupied sites. Applying the pseudo-steady state hypothesis to the relevant reactive intermediates (OOH*, OH*, O*, $H^{\#}$) yields a rate expression predicting a linear H_2O_2 formation dependence on $[H_2]$ before saturation, consistent with experimental data obtained from Pd nanoparticles supported on microporous (Pd-FAU) and mesoporous (Pd-Al-MCM-41) aluminosilicates (Fig. 4) as well as prior silica supported Pd catalysts.[6,10–12,23]

Fig. 5 shows overall rates of H_2 oxidation ($-r_{H_2} = r_{H_2O_2} + r_{H_2O}$) and HD formation rates (r_{HD}) as functions of H_2 and D_2 pressures for Pd–SiO_2 and Pd-FAU-15 catalysts (10–200 kPa H_2, 10–200 kPa D_2, 60 kPa O_2, 286 K). Comparisons among H_2 oxidation and HD formation rates give evidence for the reversibility of hydrogen activation and hydrogen coverages during catalysis. At lower pressures of hydrogen and deuterium, H_2O_2 and H_2O formation rates on Pd–SiO_2 increase linearly, which indicates hydrogen and deuterium atoms (H*-atoms, D*-atoms) exist at low coverages on Pd active sites. At higher pressures, H_2O_2 and H_2O formation rates approach constant values and HD rates increase linearly and reveal that H*- and D*-atoms achieve saturation coverages under these conditions. The comparison of r_{HD} with $r_{H_2O_2}$ and r_{H_2O} demonstrate also that H_2 activation

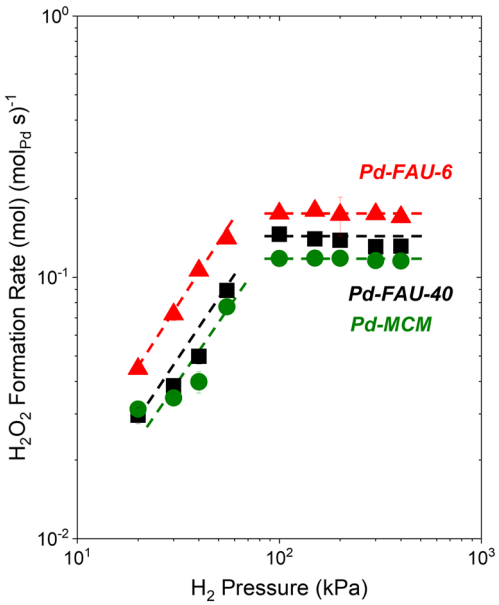

Fig. 4 H_2O_2 formation rates as a function of H_2 pressure (20–400 kPa H_2, 60 kPa O_2, 286 K) on Pd-FAU-6 (red ▲), Pd-FAU-40 (black ■), and Pd-MCM (green ●).

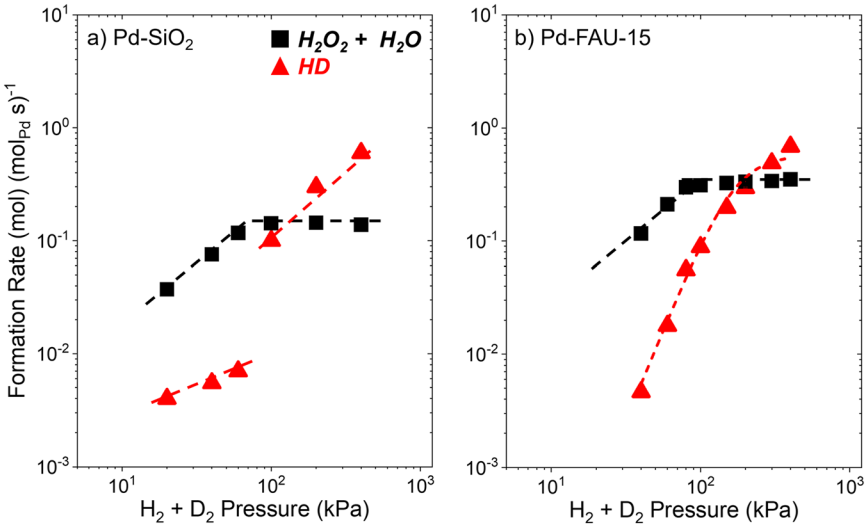

Fig. 5 H_2O_2 + H_2O (black ■) and HD (red ▲) formation rates as a function of H_2 + D_2 pressure (10–200 kPa H_2, 10–200 kPa D_2, 60 kPa O_2, 286 K) on (a) Pd–SiO_2 and (b) Pd-FAU-15 catalyst reduced *ex situ* at 773 K. H_2 and D_2 were fed in equimolar quantities.

occurs with limited reversibility at low pressures and approaches quasi-equilibrium at the highest H_2 pressures in Pd–SiO_2. Over Pd-FAU, comparisons between values of $r_{H_2O_2}$ + r_{H_2O} and r_{HD} across the full range of conditions show that the activation of hydrogen (or deuterium) proceeds in a largely irreversible manner at lower pressures and becomes increasingly reversible (but never quasi-equilibrated) at higher pressures, as shown by r_{HD} values that only surpass values for $r_{H_2O_2}$ + r_{H_2O} by even a small margin at the greatest pressures.[52,85] These differences between Pd–SiO_2 and Pd-FAU indicate that the mechanisms for H_2O_2 and H_2O formation remain consistent across supports, however, differences in the kinetic relevance of H_2 activation appear with the introduction of Brønsted acid sites. Most significantly, the lower reversibility of hydrogen activation on Pd-FAU, compared with Pd–SiO_2, suggests the involvement of H^+ from the Brønsted acid supports in forming H_2O_2 and H_2O, in addition to chemisorbed hydrogen from hydrogen or deuterium gases. This additional involvement of the Brønsted acid sites likely changes the binding energies of hydrogen or deuterium, thereby decreasing the reversibility of H_2 activation.

The previously established mechanism and rate expressions[10–12,23,52] appears consistent with all observations for these materials (detailed derivation in Section S6). The rate expression for H_2 consumption takes the following form at high H_2 pressures ($^{\#}$ – sites covered by H atoms),

$$-r_{H_2} = k_3K_2[O_2] \quad (1)$$

where values of $-r_{H_2}$ do not depend explicitly on the rate constant for H_2 activation (k_1, because step 1 precedes the kinetically relevant step) and reflects the equilibrium constant for O_2 adsorption (K_2) and the rate constant for subsequent reduction to OOH* (k_3). The rate expressions for H_2O_2 and H_2O formation take similar forms:

$$r_{H_2O_2} = \frac{k_3k_4K_2}{k_4 + 2k_5}[O_2] \quad (2)$$

and

$$r_{H_2O} = \frac{2k_3k_5K_2}{k_4 + 2k_5}[O_2] \quad (3)$$

which contains terms that reflect the generation of reactive intermediates (k_3K_2) as well as the selectivity of OOH* reduction to each pathway (k_4 and k_5). These rate expressions (eqn (2) and (3)) remain difficult to interpret molecularly, however, the ratio of the H_2O_2 and H_2O formation rates relates directly to the ratio of rate constants that govern the pathways that consume the common OOH* intermediate:

$$\frac{r_{H_2O_2}}{r_{H_2O}} = \frac{k_4}{2k_5} \quad (4)$$

This rate ratio may be restated in a form suggested by transition state theory as an explicit function of intrinsic activation enthalpies ($\Delta H_i^{\ddagger}$) and entropies ($\Delta S_i^{\ddagger}$) for individual elementary steps i:

$$\frac{r_{H_2O_2}}{r_{H_2O}} = \frac{k_4}{2k_5} = \frac{1}{2}e^{\frac{\left(\Delta G_5^{\ddagger} - \Delta G_4^{\ddagger}\right)}{RT}} = \frac{1}{2}e^{\frac{\left(\Delta S_4^{\ddagger} - \Delta S_5^{\ddagger}\right)}{R}} \cdot e^{\frac{\left(\Delta H_5^{\ddagger} - \Delta H_4^{\ddagger}\right)}{RT}} \quad (5)$$

This form shows that the differences between the apparent activation enthalpies for H_2O_2 $\left(\Delta S_{H_2O_2}^{\ddagger}\right)$ and H_2O $\left(\Delta H_{H_2O}^{\ddagger}\right)$ formation observed across Pd-zeolite catalysts equal the differences between intrinsic activation enthalpies of steps 4 ($\Delta H_4^{\ddagger}$) and 5 ($\Delta H_5^{\ddagger}$), while analogous equalities describe values of $\Delta S_i^{\ddagger}$.

$$\Delta\Delta H^{\ddagger} = \Delta H_{H_2O}^{\ddagger} - \Delta H_{H_2O_2}^{\ddagger} = \Delta H_5^{\ddagger} - \Delta H_4^{\ddagger} \quad (6)$$

The relationship shown in eqn (6) demonstrates that measured values of $\Delta\Delta H^{\ddagger}$ and comparison among Pd-zeolites provide a molecularly sensitive descriptor to learn how the

catalytic reduction of O_2 with H_2 responds to differences at the interface between Pd nanoparticles and the local liquid phase.

3.4. Effects of acid site concentration and local pH on rates, activation enthalpies, and entropies

Comparisons among rates and selectivities for H_2O_2 and H_2O formation (Fig. 1) over a series of supported Pd nanoparticle catalysts demonstrate that pore structure and the presence of Brønsted acid functions of the support influence performance. Consistent values for apparent activation enthalpies (*i.e.*, $\Delta H^{\ddagger}_{H_2O}$, $\Delta H^{\ddagger}_{H_2O_2}$) across a series of Pd-FAU catalysts created by distinct thermal treatments (Fig. 2), together with infrared spectra of CO* strongly suggest that Pd nanoparticles, and not isolated cationic Pd atoms catalyze O_2 reduction with H_2. These reactions proceed *via* proton–electron transfer steps mediated by solvent H_2O on H-saturated surfaces, following previously established mechanism for Pd-based catalysts[10–12,23,52] based on reactant pressure dependencies (Fig. 4 and 5). Collectively, these observations imply that variations in ionic strength, local pH, or hydrogen-bonding among water molecules near Pd active sites lead to the observed differences in reactivity among supported Pd catalyst.

The local pH or ionic strength of the reaction environment could alter the rates or barriers for the formation of H_2O_2 and H_2O either by controlling the activity of protons that participate in PET steps for O_2 reduction or by influencing the stability of reactive surface intermediates (*e.g.*, OOH*, H*).[41,45,86,87] The ionic strength of liquids confined within the micropores of zeolites depend directly upon the Si/Al ratio, which largely determines the number of H^+ and conjugate anionic charges on the framework.[40] Comparisons among H_2O_2 and H_2O rates across a series of Pd-FAU catalysts with a wide range of Si/Al ratios ($6 \leq$ Si/Al ≤ 385, Table 1) but comparable Pd content gives insight to how ionic strength affects kinetics.

Fig. 6 shows that H_2O_2 formation rates, selectivities (Fig. 6a), and values of $\Delta H^{\ddagger}_{H_2O_2}$ and $\Delta H^{\ddagger}_{H_2O}$ (Fig. 6b) vary minimally for Pd-FAU materials despite a 50-fold difference in the Si/Al ratio (200 kPa H_2, 60 kPa O_2; all catalysts reduced *ex situ* in 101 kPa H_2 at 773 K, Fig. S14 and S15 present the measurements of rates as functions of inverse temperatures). Notably, these comparisons require low loadings of Pd (0.02 wt% Pd) upon the Pd-FAU catalysts to avoid internal mass transfer limitations (Fig. S5), and the corresponding Al/Pd ratios remain greater than 10 for all FAU materials. Consequently, the Pd nanoparticles formed remain in close proximity to Al^- and clusters of hydronium ions (H_3O^+) and water. The local ionic strength may, therefore, remain unchanged and give the near-constant rates, selectivities, and apparent activation enthalpies (Fig. 6), in spite of the changes in Si/Al that increase the ionic strength of the bulk system.

For solid acids, and mixtures of heterogeneous solid acids specifically, the point of zero charge (PZC) reflects the net surface charge behavior and provides an ensemble-averaged descriptor of the proton affinity of all surface functional groups. As described previously, in aluminosilicate and oxide supports, both Brønsted and Lewis acid sites contribute to the overall acid–base behavior that determines the PZC. Materials with lower PZC values possess surface site distributions that include a greater fraction of strongly acidic Brønsted acid sites with low deprotonation energies and highly electrophilic Lewis acid sites with high electron affinity.[88] While PZC does not directly quantify the strength

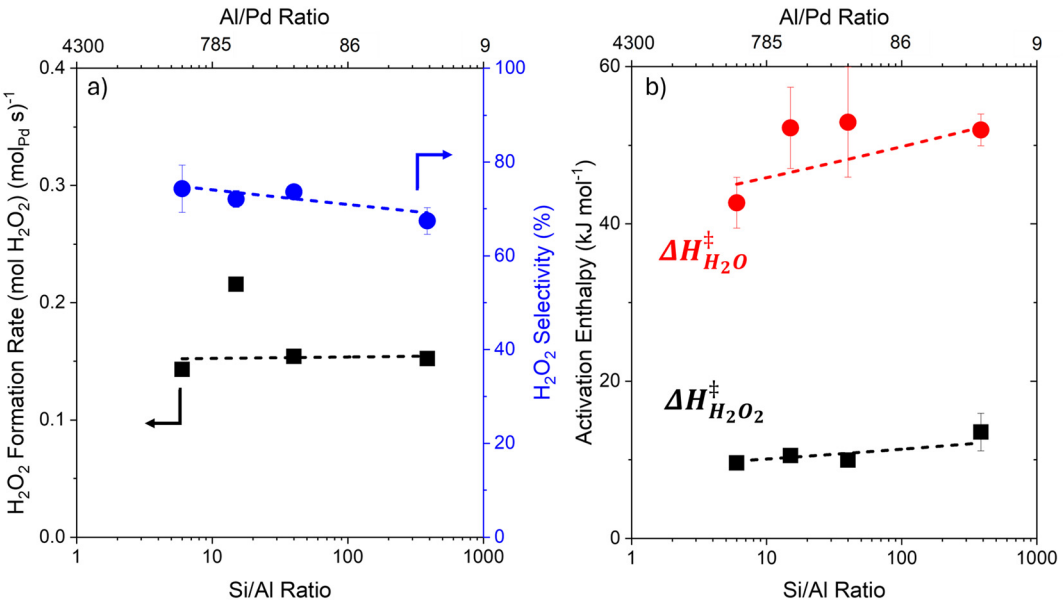

Fig. 6 (a) H_2O_2 formation rates (black ■) and selectivities (blue ●; 200 kPa H_2, 60 kPa O_2, 286 K), and (b) apparent activation enthalpies for H_2O_2 (black ■) and H_2O (red ●) formation (200 kPa H_2, 60 kPa O_2, 276–296 K) as a function of Si/Al and Al/Pd ratio for 0.02 wt% Pd-FAU materials reduced with the intent to form nanoparticles prior to catalysis (101 kPa H_2, 773 K).

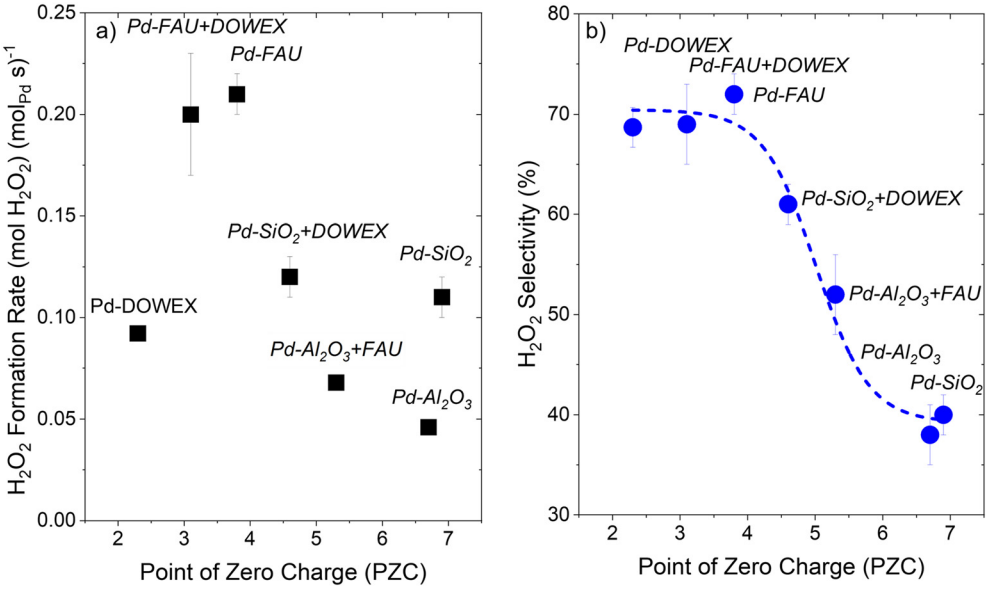

Fig. 7 (a) H_2O_2 formation rates (black) and (b) selectivities (blue) on selected catalysts and physical mixtures of catalyst with solid acid materials and their point of zero charge (200 kPa H_2, 60 kPa O_2, 286 K).

of individual acid sites, these values offer a useful metric of average acidity in complex solids and mixtures.[87,89–93] Fig. 7 compares steady state H_2O_2 formation rates (Fig. 7a) and selectivities (Fig. 7b) on Pd–Al_2O_3, Pd–SiO_2 and Pd-FAU to those obtained from physical mixtures of the same materials with a solid acid added to decrease the bulk solution pH. Physical mixtures of Pd–Al_2O_3 and H-FAU were prepared by combining equal masses (~900 mg) of each material (particles diameters <75 μm) into 250–500 μm aggregates, whereas sulfonic acid resin particles (DOWEX, 300–500 μm resin beads) were physically mixed with similarly sized (250–500 μm) aggregates of Pd–SiO_2 or Pd-FAU. The diameters of these support particles in each physical mixture ensure that adding the solid acid mainly affects the solution pH and proton activity, rather than differences in surface moieties proximate to Pd nanoparticles that influence hydrogen bonding of water at the interface.

The physical mixture of H-FAU and Pd–Al_2O_3 provides greater rates and selectivities compared to Pd–Al_2O_3 alone: H_2O_2 formation rates increase modestly from 0.05 to 0.07 mol mol_{Pd}^{-1} s^{-1} and H_2O_2 selectivities rise from 38% to 52%. The results appear qualitatively consistent with previous studies on the effects of adding mineral acids (*e.g.*, H_2SO_4, H_3PO_4, HCl) to aqueous solvents during direct synthesis of H_2O_2 to supported Pd nanoparticles.[4] Similarly, Pd–SiO_2 physically mixed with DOWEX provides a selectivity of 61% compared to 40% for Pd–SiO_2 alone, while H_2O_2 formation rates remain comparable. In contrast, Pd-FAU and physical mixtures of Pd-FAU with DOWEX give both H_2O_2 formation rates and selectivities indistinguishable from those on Pd-FAU. The absence of an additional promotional effect on Pd-FAU catalysts indicates that the incremental change in solution pH from adding the sulfonic acid has minimal impact on catalysis at Pd nanoparticles. The data from physical mixture experiments (Fig. 7) also suggest that the proximity of Pd to Brønsted acid sites and any resulting local concentration gradients do not significantly influence H_2O_2 rates and selectivity. Collectively, these comparisons show that microporous aluminosilicate supports with lower PZC and greater fractions of Brønsted and Lewis acid sites increase H_2O_2 selectivities by lowering the solution pH (increasing the activity of protons) and not through local interactions between the water solvent and either framework Al-atoms or the anionic moieties on the zeolites, while H_2O_2 formation rates remain agnostic to solution pH. The reasons selectivities depend on solution pH require further knowledge of the reaction kinetics, which comes from measured values of $\Delta H^{\ddagger}_{H_2O_2}$ and $\Delta H^{\ddagger}_{H_2O}$ across the same series of materials and physical mixtures.

Transition state theory provides a framework for interpreting apparent activation enthalpy measurements performed on different catalysts within the same coverage regime as descriptors of catalytic reactivity. Scheme S2 shows a qualitative reaction coordinate diagram illustrating the physical significance of the measurable apparent activation enthalpies consistent with the current understanding of the H_2O_2 synthesis mechanism. The activation enthalpy measurements were performed under conditions that saturate the Pd nanoparticle surface with hydrogen-atoms (Fig. 4) and hydrogen activation proceeds reversibly. Further, the difference between the apparent activation enthalpies for H_2O_2 and for H_2O formation $\left(\Delta\Delta H^{\ddagger} = \Delta H^{\ddagger}_{H_2O} - \Delta H^{\ddagger}_{H_2O_2}\right)$ reflects the difference in absolute enthalpy between the transition states.

Fig. 8a shows that values of $\Delta H^{\ddagger}_{H_2O_2}$, $\Delta H^{\ddagger}_{H_2O}$, and $\Delta H^{\ddagger}_{H_2}$ increase monotonically as PZC values decrease for the diverse series of materials examined here (all samples from Table 1,

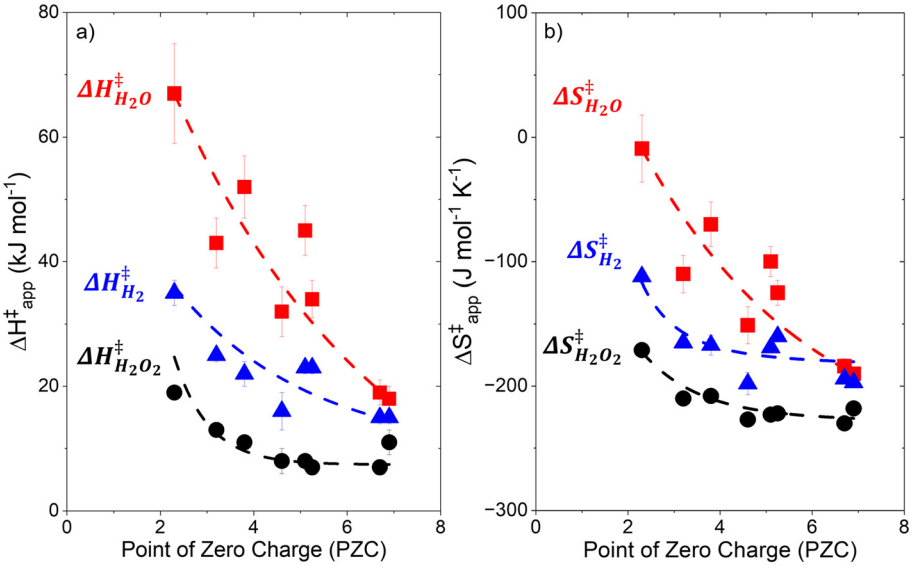

Fig. 8 Measured apparent activation (a) enthalpies and (b) entropies for the formation of H_2O_2 (black ●) and H_2O (red ■) and the consumption of H_2 (blue ▲) as a function of the point of zero charge (PZC) across supported Pd catalysts and physical mixtures of supported Pd catalysts with solid acids (200 kPa H_2, 60 kPa O_2, 276–296 K). Aluminosilicate-supported Pd catalysts were reduced *ex situ* at 773 K prior to catalysis.

Fig. S16–S23 present the measurements of rates as functions of inverse temperatures). Among these, values of $\Delta H^{\ddagger}_{H_2O}$ and $\Delta H^{\ddagger}_{H_2}$ sense the PZC most strongly and differ by a large value across materials (~50 kJ mol^{-1}), whereas $\Delta H^{\ddagger}_{H_2O_2}$ values increase modestly (~10 kJ mol^{-1}). Catalysts comprised of Pd nanoparticles supported on Brønsted acidic aluminosilicates show slightly higher $\Delta H^{\ddagger}_{H_2O_2}$ values (8–14 kJ mol^{-1}) than Pd–SiO_2 and Pd–Al_2O_3 (7–10 kJ mol^{-1}). Meanwhile, $\Delta H^{\ddagger}_{H_2O}$ values for Pd within aluminosilicate materials (*e.g.*, BEA, MCM, FAU) exceed those for Pd–SiO_2 and Pd–Al_2O_3 by ~30 kJ mol^{-1}. These comparisons show that Brønsted acidic supports increase H_2O_2 selectivities by preferentially destabilizing the H_2O formation transition state due to a lower local pH at the Pd active sites.

Increasingly positive apparent activation entropies compensate for the gains in apparent activation enthalpies observed for materials that possess lower PZC values. Fig. 8b shows the apparent activation entropies for H_2O_2 formation $\left(\Delta S^{\ddagger}_{H_2O_2}\right)$, H_2O formation $\left(\Delta S^{\ddagger}_{H_2O}\right)$, and for H_2 consumption $\left(\Delta S^{\ddagger}_{H_2}\right)$ increase as the PZC of the support or the physical mixture of the support and a secondary Brønsted acidic material decreases (SI S7 details methods of calculation). Comparisons between the apparent activation enthalpy and entropy indicate that entropic effects largely offset the increasing enthalpic effects as PZC values decrease (Fig. S25). For example, an increase in $\Delta H^{\ddagger}_{H_2O_2}$ of ~10 kJ mol^{-1} with decreasing PZC accompanies an increase in $\Delta S^{\ddagger}_{H_2O_2}$ of ~50 J mol^{-1} K^{-1} across the range of materials examined. Compared to H_2O_2, $\Delta S^{\ddagger}_{H_2O}$ increases by a greater amount (~90 J mol^{-1} K^{-1}) and offsets an increase in $\Delta H^{\ddagger}_{H_2O}$ by ~50 kJ mol^{-1} with a decrease in PZC from 6.9 to 2.3. These comparisons demonstrate that the transition states responsible for the formation of H_2O sense the physical changes within the local environment of Pd nanoparticles more strongly than those that generate H_2O_2 or activate H_2.

Recent studies highlight the role of pH on modifying the near-surface electric fields which are ubiquitous in catalysis and arise from adsorbate-induced double-layer polarization.[43,94] These fields develop concomitantly with changes in the solvent structure,[42] potentially impacting binding energies.[95–97] The binding energy for hydrogen atoms on Pt, Pd, and other transition metal catalysts decrease systematically as local pH values decrease (*i.e.*, proton concentrations increase), as demonstrated in electrochemical studies through cyclic voltammetry,[45,46] and thermochemistry in H_2-D_2O exchange experiments.[98] Correspondingly, findings from Fig. 8a suggest that O_2^* and OOH* bind more weakly to Pd surfaces in increasingly acidic environments according to Hammond's postulate.[99] Bond order conservation principles[100,101] indicate that weaker binding of OOH* increases the apparent activation enthalpy for water formation (*i.e.*, $\Delta H^{\ddagger}_{H_2O}$), thus suppressing O–O bond scission and enhancing H_2O_2 selectivities.[102,103] The values for all $\Delta H^{\ddagger}$ in Fig. 8a align with these expectations, supporting the idea that the observed changes in rates and selectivities follow classical linear free energy scaling relations. A decrease in the binding energy of the key hydroperoxyl (OOH*) intermediate on Pd surfaces in acidic solutions could therefore explain the promotional effect of acidity observed in zeolite and sulfonic acid resin-supported Pd catalysts for H_2O_2 synthesis from H_2 and O_2.[102,103]

Beyond changes to metal-adsorbate binding, the preferential enthalpic destabilization of H_2O formation transition states (and associated entropic differences) may

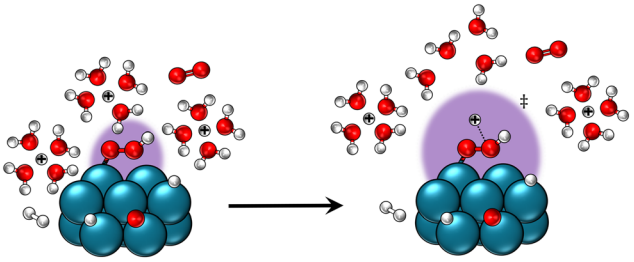

Scheme 2 Scheme depicts the displacement of solvated protons and void creation for the H_2O transition state on Pd catalysts supported on low PZC supports or low pH environments.

also be considered a consequence of outer-sphere interactions. The difference among the values of material PZC (and corresponding difference of 4.6 pH units of the solution) signifies a reduction in catalyst potential of ~270 mV, as predicted by the reversible hydrogen electrode model for fixed coverages of $H^{\#}$ and O* and constant H_2 and O_2 pressures. Consequently, lower PZC values (and local pH values) will produce stronger interfacial electric fields and more strongly organize networks of hydronium ions and water near the Pd surface and the adsorbed OOH* that reacts to form both H_2O and H_2O_2.[41,42,95,98,104–107] The greater span of $\Delta H^{\ddagger}_{H_2O}$ and $\Delta S^{\ddagger}_{H_2O}$ values relative to H_2O_2 formation agree with expectations that the H_2O formation transition state occupies a greater volume and presents a larger dipole than that for H_2O_2 formation, and as such, responds more sensitively to pH-induced changes to the solvent structure and electric field at the surface. Notably, creation of either transition state requires displacing solvated protons from the near surface region, and the larger transition state that produces H_2O and O* should necessitate the formation of a greater void within the electrical double layer present at the nanoparticle surface, as depicted in Scheme 2. These solvent-mediated effects preferentially stabilize OOH* and suppress O–O bond scission, which explains the greater H_2O_2 selectivities with more acidic supports and environments. Scatter plots relating $\Delta S^{\ddagger}$ to $\Delta H^{\ddagger}$ (Fig. S25) indicate that the kinetic parameters for H_2O_2 formation, H_2O formation, and H_2 consumption reactions show enthalpy-entropy compensation or a high degree of collinearity (*i.e.*, the best fit lines to $\Delta S^{\ddagger}$ to $\Delta H^{\ddagger}$ for each reaction show nearly identical slopes and intercepts). These non-covalent interactions between the zeolite framework, solvent H_2O molecules, solvated H_3O^+ ions, adsorbates, and transition states, appear to play a key role in determining H_2O_2 rates and selectivity. These results help elucidate the role of zeolite supports and the significance of solution and interfacial pH in the direct synthesis of H_2O_2, which provides valuable insight for the rational design of efficient catalysts.

4. Conclusions

Pd supported on zeolites and sulfonic acid resins exhibit greater rates and selectivities towards H_2O_2 compared to Pd upon Al_2O_3 and SiO_2, which lack strong Brønsted acid sites. Zeolites stabilize both Pd single-atoms and nanoparticles, yet only Pd nanoparticles contribute measurably to rates of H_2O_2 and H_2O formation *via* the catalytic reduction of O_2 with H_2. H_2O_2 formation rates on Pd supported on zeolites vary systematically with pore diameter, suggesting that confinement within the zeolite framework plays a key role in governing catalyst reactivity. Selectivities toward H_2O_2, however, appear largely independent of zeolite topology but depend strongly upon point of zero charge (a functional probe of acid strength) for the combination of solid catalysts utilized, which influences the pH of the solution near Pd active sites. Both H_2O_2 and H_2O derive from common OOH* intermediates, and as such, measurements of apparent activation enthalpies ($\Delta H^{\ddagger}_{H_2O_2}$, $\Delta H^{\ddagger}_{H_2O}$) and entropies ($\Delta S^{\ddagger}_{H_2O_2}$, $\Delta S^{\ddagger}_{H_2O}$) reveal that decreases in local pH preferentially destabilize transition states for H_2O formation over those that form H_2O_2. This destabilization appears most clearly when H-atoms, and not oxygen derived intermediates, saturate Pd surfaces and imply that outer-sphere interactions control selectivity between these competing pathways.

Prior literature on zeolite and Brønsted acid catalysts for H_2O_2 direct synthesis establishes that Brønsted acid supports play an active role in the chemistry beyond the capabilities of traditional metal oxide supports. Confinement of metals within acidic zeolite frameworks has been shown to enhance H_2O_2 selectivity by facilitating proton transfer pathways, suppressing H_2O_2 decomposition, and promoting H_2 activation, analogous to mineral acid promoters. These studies often involve acid, organic, halide promoters, or combinations of these, which complicates isolating the effects attributable solely to Brønsted acid supports. Consequently, there is a lack of mechanistic and molecular understanding of how Brønsted acid sites and the local solvent environment influence H_2O_2 formation rates and selectivity, and limited evidence regarding the nature of metal active sites. The findings outlined in this work reveal that metallic Pd clusters or nanoparticles located within zeolite pores or near Brønsted acid sites on the support are active for H_2O_2 production and underscore the importance of interfacial pH in guiding H_2O_2 synthesis pathways. This work offers a framework for designing catalysts that maximize selectivity through rational control of the local reaction environment for other O_2 reduction reactions.

Author contributions

T. R. and S. V. contributed equally to the manuscript. T. R. synthesized and characterized the catalysts and performed kinetic measurements. S. V. performed characterization and kinetic measurements on catalysts. J. S. A. assisted with kinetic measurements. D. W. F. conceptualized the manuscript. The manuscript was drafted by T. R. and S. V. with revisions and edits from all authors.

Conflicts of interest

There are no conflicts to declare.

Data availability

Characterization plots, supplemental kinetics, full rate derivations, apparent activation enthalpy and entropy values, and all TEM images are included in the supplementary information (SI).

Supplementary information is available. See DOI: https://doi.org/10.1039/d6cy00219f.

Acknowledgements

The authors thank Huston Locht for helpful feedback on the manuscript. ICP-OES measurements were carried out at the Microanalysis Lab at the University of Illinois. TEM measurements were performed at the Materials Characterization Facility at Georgia Institute of Technology. This work was supported by the National Science Foundation (CHE-2300019) and funds from the Georgia Institute of Technology. S. V. acknowledges the support of the Natural Sciences and Engineering Research Council of Canada (NSERC) Postgraduate Scholarship Program (PGS D-578442-2023).

References

1 J. M. Campos-Martin, G. Blanco-Brieva and J. L. G. Fierro, Hydrogen Peroxide Synthesis: An Outlook beyond the Anthraquinone Process, *Angew. Chem., Int. Ed.*, 2006, **45**(42), 6962–6984.

2 D. W. Flaherty, Direct Synthesis of H_2O_2 from H_2 and O_2 on Pd Catalysts: Current Understanding, Outstanding Questions, and Research Needs, *ACS Catal.*, 2018, **8**, 1520–1527.

3 R. J. Lewis, J. K. Edwards, S. J. Freakley and G. J. Hutchings, Solid Acid Additives as Recoverable Promoters for the Direct Synthesis of Hydrogen Peroxide, *Ind. Eng. Chem. Res.*, 2017, **56**(45), 13287–13293, DOI: 10.1021/acs.iecr.7b01800.

4 N. M. Wilson and D. W. Flaherty, Mechanism for the Direct Synthesis of H_2O_2 on Pd Clusters: Heterolytic Reaction Pathways at the Liquid–Solid Interface, *J. Am. Chem. Soc.*, 2016, **138**(2), 574–586, DOI: 10.1021/jacs.5b10669.

5 G. Gallina, J. García-Serna, T. O. Salmi, P. Canu and P. Biasi, Bromide and Acids: A Comprehensive Study on Their Role on the Hydrogen Peroxide Direct Synthesis, *Ind. Eng. Chem. Res.*, 2017, **56**(45), 13367–13378, DOI: 10.1021/acs.iecr.7b01989.

6 P. Priyadarshini, T. Ricciardulli, J. S. Adams, Y. S. Yun and D. W. Flaherty, Effects of bromide adsorption on the direct synthesis of H_2O_2 on Pd nanoparticles: Formation rates, selectivities, and apparent barriers at steady-state, *J. Catal.*, 2021, **399**, 24–40, DOI: 10.1016/j.jcat.2021.04.020.

7 C. Samanta, Direct synthesis of hydrogen peroxide from hydrogen and oxygen: An overview of recent developments in the process, *Appl. Catal., A*, 2008, **350**(2), 133–149, DOI: 10.1016/j.apcata.2008.07.043.

8 Y.-F. Han and J. H. Lunsford, Direct formation of H_2O_2 from H_2 and O_2 over a Pd/SiO_2 catalyst: the roles of the acid and the liquid phase, *J. Catal.*, 2005, **230**(2), 313–316.

9 Q. Liu and J. H. Lunsford, Controlling factors in the direct formation of H_2O_2 from H_2 and O_2 over a Pd/SiO_2 catalyst in ethanol, *Appl. Catal., A*, 2006, **314**(1), 94–100.

10 J. S. Adams, A. Chemburkar, P. Priyadarshini, T. Ricciardulli, Y. Lu, V. Maliekkal, A. Sampath, S. Winikoff, A. M. Karim and M. Neurock, Solvent molecules form surface redox mediators in situ and cocatalyze O_2 reduction on Pd, *Science*, 2021, **371**(6529), 626–632.

11 T. Ricciardulli, S. Gorthy, J. S. Adams, C. Thompson, A. M. Karim, M. Neurock and D. W. Flaherty, Effect of Pd Coordination and Isolation on the Catalytic Reduction of O_2 to H_2O_2 over PdAu Bimetallic Nanoparticles, *J. Am. Chem. Soc.*, 2021, **143**(14), 5445–5464, DOI: 10.1021/jacs.1c00539.

12 T. Ricciardulli, J. S. Adams, M. DeRidder, A. P. v. Bavel, A. M. Karim and D. W. Flaherty, H_2O-assisted O_2 reduction by H_2 on Pt and PtAu bimetallic nanoparticles: Influences of composition and reactant coverages on kinetic regimes, rates, and selectivities, *J. Catal.*, 2021, **404**, 661–678.

13 S. J. Freakley, Q. He, J. H. Harrhy, L. Lu, D. A. Crole, D. J. Morgan, E. N. Ntainjua, J. K. Edwards, A. F. Carley and A. Y. Borisevich, Palladium-tin catalysts for the direct synthesis of H_2O_2 with high selectivity, *Science*, 2016, **351**(6276), 965–968.

14 S. Wang, D. E. Doronkin, M. Hähsler, X. Huang, D. Wang, J. D. Grunwaldt and S. Behrens, Palladium-based bimetallic nanocrystal catalysts for the direct synthesis of hydrogen peroxide, *ChemSusChem*, 2020, **13**(12), 3243–3251.

15 J. K. Edwards, E. N. Ntainjua, A. F. Carley, A. A. Herzing, C. J. Kiely and G. J. Hutchings, Direct Synthesis of H_2O_2 from H_2 and O_2 over Gold, Palladium, and Gold–Palladium Catalysts Supported on Acid-Pretreated TiO_2, *Angew. Chem., Int. Ed.*, 2009, **48**(45), 8512–8515.

16 J. K. Edwards, A. Thomas, A. F. Carley, A. A. Herzing, C. J. Kiely and G. J. Hutchings, Au–Pd supported nanocrystals as catalysts for the direct synthesis of hydrogen peroxide from H_2 and O_2, *Green Chem.*, 2008, **10**(4), 388–394, DOI: 10.1039/B714553P.

17 J. Gu, S. Wang, Z. He, Y. Han and J. Zhang, Direct synthesis of hydrogen peroxide from hydrogen and oxygen over activated-carbon-supported Pd–Ag alloy catalysts, *Catal. Sci. Technol.*, 2016, **6**(3), 809–817, DOI: 10.1039/C5CY00813A.

18 R. Svensson and H. Gronbeck, Site communication in direct formation of H_2O_2 over single-atom Pd@ Au nanoparticles, *J. Am. Chem. Soc.*, 2023, **145**(21), 11579–11588.

19 R. T. Hannagan, G. Giannakakis, M. Flytzani-Stephanopoulos and E. C. H. Sykes, Single-Atom Alloy Catalysis, *Chem. Rev.*, 2020, **120**(21), 12044–12088.

20 L. F. d. L. e. Freitas, B. Puértolas, J. Zhang, B. Wang, A. S. Hoffman, S. R. Bare, J. Pérez-Ramírez, J. W. Medlin and E.

NikollaTunable Catalytic Performance of Palladium Nanoparticles for H_2O_2 Direct Synthesis via Surface-Bound Ligands, *ACS Catal.*, 2020, **10**(9), 5202–5207.

21 G. M. Lari, B. Puértolas, M. Shahrokhi, N. López and J. Pérez-Ramírez, Hybrid palladium nanoparticles for direct hydrogen peroxide synthesis: the key role of the ligand, *Angew. Chem.*, 2017, **129**(7), 1801–1805.

22 A. H. Jenkins, C. B. Musgrave and J. W. Medlin, Altering Linear Scaling Relationships on Metal Catalysts via Ligand–Adsorbate Hydrogen Bonding, *J. Phys. Chem. C*, 2021, **125**(43), 23791–23808.

23 J. S. Adams, M. Tanwar, H. Chen, S. Vijayaraghavan, T. Ricciardulli, M. Neurock and D. W. Flaherty, Intentional Formation of Persistent Surface Redox Mediators by Adsorption of Polyconjugated Carbonyl Complexes to Pd Nanoparticles, *J. Am. Chem. Soc.*, 2025, **147**(20), 16885–16900, DOI: 10.1021/jacs.4c15874.

24 J. H. Lunsford, The direct formation of H_2O_2 from H_2 and O_2 over palladium catalysts, *J. Catal.*, 2003, **216**(1–2), 455–460.

25 S. Eckstein, P. H. Hintermeier, R. Zhao, E. Baráth, H. Shi, Y. Liu and J. A. Lercher, Influence of Hydronium Ions in Zeolites on Sorption, *Angew. Chem., Int. Ed.*, 2019, **58**(11), 3450–3455.

26 S. Park, S. H. Lee, S. H. Song, D. R. Park, S.-H. Baeck, T. J. Kim, Y.-M. Chung, S.-H. Oh and I. K. Song, Direct synthesis of hydrogen peroxide from hydrogen and oxygen over palladium-exchanged insoluble heteropolyacid catalysts, *Catal. Commun.*, 2009, **10**(4), 391–394.

27 J. W. Lee, J. K. Kim, T. H. Kang, E. J. Lee and I. K. Song, Direct synthesis of hydrogen peroxide from hydrogen and oxygen over palladium catalyst supported on heteropolyacid-containing ordered mesoporous carbon, *Catal. Today*, 2017, **293–294**, 49–55.

28 K. Mori, K. Furubayashi, S. Okada and H. Yamashita, Synthesis of Pd nanoparticles on heteropolyacid-supported silica by a photo-assisted deposition method: an active catalyst for the direct synthesis of hydrogen peroxide, *RSC Adv.*, 2012, **2**, 1047–1054.

29 P. Biasi, P. Canu, F. Menegazzo, F. Pinna and T. O. Salmi, Direct Synthesis of Hydrogen Peroxide in a Trickle Bed Reactor: Comparison of Pd-Based Catalysts, *Ind. Eng. Chem. Res.*, 2012, **51**(26), 8883–8890.

30 F. Menegazzo, M. Signoretto, M. Manzoli, F. Boccuzzi, G. Cruciani, F. Pinna and G. Strukul, Influence of the preparation method on the morphological and composition properties of Pd–Au/ZrO_2 catalysts and their effect on the direct synthesis of hydrogen peroxide from hydrogen and oxygen, *J. Catal.*, 2009, **268**(1), 122–130.

31 G. Bernardotto, F. Menegazzo, F. Pinna, M. Signoretto, G. Cruciani and G. Strukul, New Pd–Pt and Pd–Au catalysts for an efficient synthesis of H_2O_2 from H_2 and O_2 under very mild conditions, *Appl. Catal., A*, 2009, **358**(2), 129–135.

32 C. Burato, S. Campestrini, Y.-F. Han, P. Canton, P. Centomo, P. Canu and B. Corain, Chemoselective and re-usable heterogeneous catalysts for the direct synthesis of hydrogen peroxide in the liquid phase under non-explosive conditions and in the absence of chemoselectivity enhancers, *Appl. Catal., A*, 2009, **358**(2), 224–231.

33 G. Blanco-Brieva, F. Desmedt, P. Miquel, J. M. Campos-Martin and J. L. G. Fierro, Direct synthesis of hydrogen peroxide without the use of acids or halide promoters in dissolution, *Catal. Sci. Technol.*, 2020, **10**, 2333–2336.

34 G. Blanco-Brieva, M. Montiel-Argaiz, F. Desmedt, P. Miquel, J. M. Campos-Martin and J. L. G. Fierro, Direct synthesis of hydrogen peroxide with no ionic halides in solution, *RSC Adv.*, 2016, **6**(101), 99291–99296.

35 G. Blanco-Brieva, E. Cano-Serrano, J. M. Campos-Martin and J. L. G. Fierro, Direct synthesis of hydrogen peroxide solution with palladium-loaded sulfonic acid polystyrene resins, *Catal. Commun.*, 2004, **10**, 1184–1185.

36 Z. Jin, Y. Liu, L. Wang, C. Wang, Z. Wu, Q. Zhu, L. Wang and F.-S. Xiao, Direct Synthesis of Pure Aqueous H_2O_2 Solution within Aluminosilicate Zeolite Crystals, *ACS Catal.*, 2021, **11**(4), 1946–1951, DOI: 10.1021/acscatal.0c05103.

37 Y. Liu, Z. Liu, J. Zhang, F. S. Xiao, X. Cao and L. Wang, Efficient catalytic production of hydrogen peroxide using tin-containing zeolite fixed palladium nanoparticles with oxidation resistance, *Angew. Chem., Int. Ed.*, 2023, **62**(47), e202312377.

38 D. T. Bregante, M. C. Chan, J. Z. Tan, E. Z. Ayla, C. P. Nicholas, D. Shukla and D. W. Flaherty, The shape of water in zeolites and its impact on epoxidation catalysis, *Nat. Catal.*, 2021, **4**, 797–808.

39 D. T. Bregante, A. M. Johnson, A. Y. Patel, E. Z. Ayla, M. J. Cordon, B. C. Bukowski, J. Greeley, R. Gounder and D. W. Flaherty, Cooperative Effects between Hydrophilic Pores and Solvents: Catalytic Consequences of Hydrogen Bonding on Alkene Epoxidation in Zeolites, *J. Am. Chem. Soc.*, 2019, **141**, 7302–7319.

40 N. Pfriem, P. H. Hintermeier, S. Eckstein, S. Kim, Q. Liu, H. Shi, L. Milakovic, Y. Liu, G. L. Haller and E. Baráth, *et al.*, Role of the ionic environment in enhancing the activity of reacting molecules in zeolite pores, *Science*, 2021, **372**(6545), 952–957.

41 X. Yang, J. Nash, N. Oliveira, Y. Yan and B. Xu, Understanding the pH dependence of underpotential deposited hydrogen on platinum, *Angew. Chem.*, 2019, **131**(49), 17882–17887.

42 S. Zhu, X. Qin, Y. Yao and M. Shao, pH-Dependent Hydrogen and Water Binding Energies on Platinum Surfaces as Directly Probed through Surface-Enhanced Infrared Absorption Spectroscopy, *J. Am. Chem. Soc.*, 2020, **142**(19), 8748–8754.

43 T. S. Wesley, Y. Román-Leshkov and Y. Surendranath, Spontaneous Electric Fields Play a Key Role in Thermochemical Catalysis at Metal–Liquid Interfaces, *ACS Cent. Sci.*, 2021, **7**(6), 1045–1055.

44 J. Ryu and Y. Surendranath, Tracking Electrical Fields at the Pt/H_2O Interface during Hydrogen Catalysis, *J. Am. Chem. Soc.*, 2019, **141**(39), 15524–15531.

45 J. Zheng, W. Sheng, Z. Zhuang, B. Xu and Y. Yan, Universal dependence of hydrogen oxidation and evolution reaction activity of platinum-group metals on pH and hydrogen binding energy, *Sci. Adv.*, 2016, **2**(3), e1501602.

46 W. Sheng, Z. Zhuang, M. Gao, J. Zheng, J. G. Chen and Y. Yan, Correlating hydrogen oxidation and evolution activity on platinum at different pH with measured hydrogen binding energy, *Nat. Commun.*, 2015, **6**, 5848.

47 R. J. Lewis, E. N. Ntainjua, D. J. Morgan, T. E. Davies, A. F. Carley, S. J. Freakley and G. J. Hutchings, Improving the performance of Pd based catalysts for the direct synthesis of hydrogen peroxide via acid incorporation during catalyst synthesis, *Catal. Commun.*, 2021, **161**, 106358.

48 J. K. Edwards, B. Solsona, E. N. Ntainjua, A. F. Carley, A. A. Herzing, C. J. Kiely and G. J. Hutchings, Switching Off Hydrogen Peroxide Hydrogenation in the Direct Synthesis Process, *Science*, 2009, **323**(5917), 1037–1041.

49 S. T. Homeyer and W. M. H. Sachtler, Oxidative Redispersion of Palladium and Formation of PdO Particles in NaY An Application of High Precision TPR, *Appl. Catal.*, 1989, **54**, 189–202.

50 J. S. Noh and J. A. Schwarz, Estimation of the point of zero charge of simple oxides by mass titration, *J. Colloid Interface Sci.*, 1989, **130**(1), 157–164.

51 J. Park and J. R. Regalbuto, A Simple, Accurate Determination of Oxide PZC and the Strong Buffering Effect of Oxide Surfaces at Incipient Wetness, *J. Colloid Interface Sci.*, 1995, **175**(1), 239–252.

52 N. M. Wilson, P. Priyadarshini, S. Kunz and D. W. Flaherty, Direct synthesis of H_2O_2 on Pd and Au_xPd_1 clusters: Understanding the effects of alloying Pd with Au, *J. Catal.*, 2018, **357**, 163–175.

53 R. J. Madon and M. Boudart, Experimental Criterion for the Absence of Artifacts in the Measurement of Rates of Heterogeneous Catalytic Reactions, *Ind. Eng. Chem. Fundam.*, 1982, **21**, 438–447.

54 J. Wang, V. F. Kispersky, W. N. Delgass and F. H. Ribeiro, Determination of the Au active site and surface active species via *operando* transmission FTIR and isotopic transient experiments on 2.3 wt.% Au/TiO_2 for the WGS reaction, *J. Catal.*, 2012, **289**, 171–178.

55 D. W. Flaherty and A. Bhan, Improving the rigor and reproducibility of catalyst testing and evaluation in the laboratory, *J. Catal.*, 2024, **431**, 115408.

56 A. J. Hoffman, J. S. Bates, J. R. Di Iorio, S. V. Nystrom, C. T. Nimlos, R. Gounder and D. Hibbitts, Rigid Arrangements of Ionic Charge in Zeolite Frameworks Conferred by Specific Aluminum Distributions Preferentially Stabilize Alkanol Dehydration Transition States, *Angew. Chem., Int. Ed.*, 2020, **59**(42), 18686–18694, DOI: 10.1002/anie.202007790, (accessed 2026/05/20).

57 D. T. Bregante, M. C. Chan, J. Z. Tan, E. Z. Ayla, C. P. Nicholas, D. Shukla and D. W. Flaherty, The shape of water in zeolites and its impact on epoxidation catalysis, *Nat. Catal.*, 2021, **4**(9), 797–808, DOI: 10.1038/s41929-021-00672-4.

58 E. Grifoni, G. Piccini, J. A. Lercher, V.-A. Glezakou, R. Rousseau and M. Parrinello, Confinement effects and acid strength in zeolites, *Nat. Commun.*, 2021, **12**(1), 2630, DOI: 10.1038/s41467-021-22936-0.

59 J. S. Bates, B. C. Bukowski, J. Greeley and R. Gounder, Structure and solvation of confined water and water–ethanol clusters within microporous Brønsted acids and their effects on ethanol dehydration catalysis, *Chem. Sci.*, 2020, **11**(27), 7102–7122, DOI: 10.1039/D0SC02589E.

60 P. Tian, L. Ouyang, X. Xu, C. Ao, X. Xu, R. Si, X. Shen, M. Lin, J. Xu and Y.-F. Han, The origin of palladium particle size effects in the direct synthesis of H_2O_2: Is smaller better?, *J. Catal.*, 2017, **349**, 30–40, DOI: 10.1016/j.jcat.2016.12.004.

61 Q. Liu, J. C. Bauer, R. E. Schaak and J. H. Lunsford, Supported Palladium Nanoparticles: An Efficient Catalyst for the Direct Formation of H_2O_2 from H_2 and O_2, *Angew. Chem., Int. Ed.*, 2008, **47**(33), 6221–6224, DOI: 10.1002/anie.200801517, (accessed 2026/05/11).

62 Y. Ye, J. Chun, S. Park, T. J. Kim, Y.-M. Chung, S.-H. Oh, I. K. Song and J. Lee, A study of the palladium size effect on the direct synthesis of hydrogen peroxide from hydrogen and oxygen using highly uniform palladium nanoparticles supported on carbon, *Korean J. Chem. Eng.*, 2012, **29**(9), 1115–1118.

63 S. Vijayaraghavan, C. T. Waldt, R. Kumar, N. Rathi, D. D. Hibbitts and D. W. Flaherty, Nanoparticle size and composition of PdAu catalysts govern the structure and kinetics of H_2O_2 formation through O_2 reduction, *J. Catal.*, 2026, **454**, 116649, DOI: 10.1016/j.jcat.2025.116649.

64 N. Wang, X. Zhao, R. Zhang, S. Yu, Z. H. Levell, C. Wang, S. Ma, P. Zou, L. Han and J. Qin, *et al.*, Highly Selective Oxygen Reduction to Hydrogen Peroxide on a Carbon-Supported Single-Atom Pd Electrocatalyst, *ACS Catal.*, 2022, **12**(7), 4156–4164.

65 M. Ledendecker, E. Pizzutilo, G. Malta, G. V. Fortunato, K. J. J. Mayrhofer, G. J. Hutchings and S. J. Freakley, Isolated Pd Sites as Selective Catalysts for Electrochemical and Direct Hydrogen Peroxide Synthesis, *ACS Catal.*, 2020, **10**(10), 5928–5938.

66 T. M. Lardinois, K. Mandal, V. Yadav, A. Wijerathne, B. K. Bolton, H. Lippie, C. W. Li, C. Paolucci and R. Gounder, Kinetic and Thermodynamic Factors Influencing Palladium Nanoparticle Redispersion into Mononuclear Pd(II) Cations in Zeolite Supports, *J. Phys. Chem. C*, 2022, **126**(19), 8337–8353.

67 T. M. Lardinois, J. S. Bates, H. H. Lippie, C. K. Russell, J. T. Miller, H. M. Meyer III, V. Prikhodko, X. Wei and C. K. Lambert, *et al.*, Structural Interconversion between Agglomerated Palladium Domains and Mononuclear Pd(II) Cations in Chabazite Zeolites, *Chem. Mater.*, 2021, **33**(5), 1698–1713.

68 G. S. Lane, J. T. Miller, F. S. Modica and M. K. Barr, Infrared Spectroscopy of Adsorbed Carbon Monoxide on Platinum/Nonacidic Zeolite Catalysts, *J. Catal.*, 1993, **141**(2), 465–477, DOI: 10.1006/jcat.1993.1155.

69 C. Naccache, M. Primet and M. V. Mathieu, Study of Hydrogen and Carbon Monoxide Interactions with Palladium-Y Zeolite by ESR and IR Spectroscopy, in *Molecular Sieves*, Advances in Chemistry, American Chemical Society, 1973, vol. 121, pp. 266–280.

70 I. Song, I. Z. Koleva, H. A. Aleksandrov, L. Chen, J. Heo, D. Li, Y. Wang, J. Szanyi and K. Khivantsev, Ultrasmall Pd Clusters in FER Zeolite Alleviate CO Poisoning for Effective Low-Temperature Carbon Monoxide Oxidation, *J. Am. Chem. Soc.*, 2023, **145**(50), 27493–27499, DOI: 10.1021/jacs.3c08916.

71 Y. Kim, J. Sung, S. Kang, J. Lee, M.-H. Kang, S. Hwang, H. Park, J. Kim, Y. Kim and E. Lee, Uniform synthesis of palladium species confined in a small-pore zeolite via full ion-exchange investigated by cryogenic electron microscopy, *J. Mater. Chem. A*, 2021, **9**(35), 19796–19806.

72 K. Khivantsev, N. R. Jaegers, I. Z. Koleva, H. A. Aleksandrov, L. Kovarik, M. Engelhard, F. Gao, Y. W. G. N. Vayssilov and J. Szanyi, Stabilization of Super Electrophilic Pd^{+2} Cations in Small-Pore SSZ-13 Zeolite, *J. Phys. Chem. C*, 2020, **124**(1), 309–321.

73 D. Mei, F. Gao, J. Szanyi and Y. Wang, Mechanistic insight into the passive NOx adsorption in the highly dispersed Pd/HBEA zeolite, *Appl. Catal., A*, 2019, **569**, 181–189.

74 K. Khivantsev, N. R. Jaegers, L. Kovarik, S. Prodinger, M. A. Derewinski, Y. Wang, F. Gao and J. Szanyi, Palladium/Beta zeolite passive NOx adsorbers (PNA): Clarification of PNA chemistry and the effects of CO and zeolite crystallite size on PNA performance, *Appl. Catal., A*, 2019, **569**, 141–148.

75 K. Khivantsev, N. R. Jaegers, L. Kovarik, J. C. Hanson, F. Tao, Y. Tang, X. Zhang, I. Z. Koleva, H. A. Aleksandrov and G. N. Vayssilov, *et al.*, Achieving Atomic Dispersion of Highly Loaded Transition Metals in Small-Pore Zeolite SSZ-13: High-Capacity and High-Efficiency Low-Temperature CO and Passive NO_x Adsorbers, *Angew. Chem., Int. Ed.*, 2018, **57**(51), 16672–16677.

76 Y. Zheng, L. Kovarik, M. H. Engelhard, Y. Wang, Y. Wang, F. Gao and J. Szanyi, Low-Temperature Pd/Zeolite Passive NOx Adsorbers: Structure, Performance, and Adsorption Chemistry, *J. Phys. Chem. C*, 2017, **121**(29), 15793–15803.

77 Z. Zhang and W. M. H. Sachtler, FTIR study of novel Pd6 carbonyl clusters encaged in zeolite 5A, *J. Mol. Catal.*, 1991, **67**(3), 349–357.

78 L.-L. Sheu, H. K. ö. Zinger and W. H. Sachtler, Palladium Carbonyl Clusters Entrapped in NaY Zeolite Cages: Ligand Dissociation and Cluster-Wall Interactions, *J. Am. Chem. Soc.*, 1989, **111**(21), 8125–8131.

79 A. W. Aylor, L. J. Lobree, J. A. Reimer and A. T. Bell, Investigations of the Dispersion of Pd in H-ZSM-5, *J. Catal.*, 1997, **172**(2), 453–462.

80 J. Szanyi, K. W. Kuhn and W. D. Goodman, CO adsorption on Pd(111) and Pd(100): Low and high pressure correlations, *J. Vac. Sci. Technol. A*, 1993, **11**(4), 1969–1974.

81 I. V. Yudanov, R. Sahnoun, K. M. Neyman, N. Rösch, J. Hoffmann, S. Schauermann, V. Johánek, H. Unterhalt, G. Rupprechter and J. Libuda, *et al.*, CO Adsorption on Pd Nanoparticles: Density Functional and Vibrational Spectroscopy Studies, *J. Phys. Chem. B*, 2003, **107**(1), 255–264.

82 P. Priyadarshini and D. W. Flaherty, Form of the catalytically active Pd species during the direct synthesis of hydrogen peroxide, *AIChE J.*, 2019, **65**(12), e16829.

83 Q. Liu, K. K. Gath, J. C. Bauer, R. E. Schaak and J. H. Lunsford, The active phase in the direct synthesis of H_2O_2 from H_2 and O_2 over Pd/SiO_2 catalyst in a H_2SO_4/ethanol system, *Catal. Lett.*, 2009, **132**(3), 342–348.

84 V. R. Choudhary, S. D. Sansare and A. G. GaikwadDirect Oxidation of H_2 to H_2O_2 and Decomposition of H_2O_2 Over Oxidized and Reduced Pd-Containing Zeolite Catalysts in Acidic Medium, *Catal. Lett.*, 2002, **84**(1), 81–87, DOI: 10.1023/A:1021032819400.

85 S. L. Leung, D. Hibbitts, M. Gárcia-Diéguez and E. Iglesia, Binding and Exchange Reactions of Hydrogen Isotopes on Surfaces of Dispersed Pt Nanoparticles, *J. Phys. Chem. C*, 2022, **126**(8), 3923–3938.

86 W. Sheng, M. Myint, J. G. Chen and Y. Yan, Correlating the hydrogen evolution reaction activity in alkaline electrolytes with the hydrogen binding energy on monometallic surfaces, *Energy Environ. Sci.*, 2013, **6**(5), 1509–1512.

87 M. Luo and M. T. Koper, A kinetic descriptor for the electrolyte effect on the oxygen reduction kinetics on Pt (111), *Nat. Catal.*, 2022, **5**(7), 615–623.

88 R. Van Santen and G. Kramer, Reactivity theory of zeolitic broensted acidic sites, *Chem. Rev.*, 1995, **95**(3), 637–660.

89 R. A. Santen, *Theoretical heterogeneous catalysis*, World Scientific, 1991.

90 M. Hunger, Multinuclear solid-state NMR studies of acidic and non-acidic hydroxyl protons in zeolites, *Solid State Nucl. Magn. Reson.*, 1996, **6**(1), 1–29.

91 P. Deshlahra and E. Iglesia, Reactivity descriptors in acid catalysis: acid strength, proton affinity and host–guest interactions, *Chem. Commun.*, 2020, **56**(54), 7371–7398.

92 A. J. Jones and E. Iglesia, The strength of Brønsted acid sites in microporous aluminosilicates, *ACS Catal.*, 2015, **5**(10), 5741–5755.

93 J. Macht, R. T. Carr and E. Iglesia, Functional assessment of the strength of solid acid catalysts, *J. Catal.*, 2009, **264**(1), 54–66.

94 J. S. Adams, M. L. Kromer, J. Rodríguez-López and D. W. Flaherty, Unifying Concepts in Electro- and Thermocatalysis toward Hydrogen Peroxide Production, *J. Am. Chem. Soc.*, 2021, **143**(21), 7940–7957.

95 P. S. Lamoureux, A. R. Singh and K. Chan, pH Effects on Hydrogen Evolution and Oxidation over Pt(111): Insights from First-Principles, *ACS Catal.*, 2019, **9**(7), 6194–6201.

96 S. R. Kelly, C. Kirk, K. Chan and J. K. Nørskov, Electric Field Effects in Oxygen Reduction Kinetics: Rationalizing pH Dependence at the Pt(111), Au(111), and Au(100) Electrodes, *J. Phys. Chem. C*, 2020, **124**(27), 14581–14591.

97 N. Govindarajan, A. Xu and K. Chan, How pH affects electrochemical processes, *Science*, 2022, **375**(6579), 379–380.

98 G. Yang, S. A. Akhade, X. Chen, Y. Liu, M.-S. Lee, V.-A. Glezakou, R. Rousseau and J. A. Lercher, The Nature of Hydrogen Adsorption on Platinum in the Aqueous Phase, *Angew. Chem., Int. Ed.*, 2019, **58**(11), 3527–3532.
99 E. V. Anslyn and D. A. Dougherty, *Modern Physical Organic Chemistry*, University Science Books, 2006.
100 N. M. Wilson, Y.-T. Pan, Y.-T. Shao, J.-M. Zuo, H. Yang and D. W. Flaherty, Direct Synthesis of H_2O_2 on AgPt Octahedra: The Importance of Ag–Pt Coordination for High H_2O_2 Selectivity, *ACS Catal.*, 2018, **8**(4), 2280–2289.
101 I. Chorkendorff and J. W. Niemantsverdriet, *Concepts of Modern Catalysis and Kinetics*, Wiley-VCH, 2003.
102 S. Siahrostami, A. Verdaguer-Casadevall, M. Karamad, D. Deiana, P. Malacrida, B. Wickman, M. Escudero-Escribano, E. A. Paoli, R. Frydenda and T. W. Hansen, *et al.*, Enabling direct H_2O_2 production through rational electrocatalyst design, *Nat. Mater.*, 2013, **12**, 1137–1143.
103 A. Kulkarni, S. Siahrostami, A. Patel and J. K. Nørskov, Understanding Catalytic Activity Trends in the Oxygen Reduction Reaction, *Chem. Rev.*, 2018, **118**(5), 2302–2312.
104 T. Cheng, L. Wang, B. V. Merinov and W. A. Goddard, Explanation of Dramatic pH-Dependence of Hydrogen Binding on Noble Metal Electrode: Greatly Weakened Water Adsorption at High pH, *J. Am. Chem. Soc.*, 2018, **140**(25), 7787–7790.
105 W. T. Broomhead, M. Chung, K. O. Albrecht and D. W. Flaherty, Catalyst Potential Prescribes Intermediate Coverages in Thermocatalytic Gluconic Acid Oxidation on Pt Nanoparticles, *J. Am. Chem. Soc.*, 2026, **148**(18), 18746–18761.
106 J. S. Adams, M. L. Kromer, J. Rodríguez-López and D. W. Flaherty, Unifying concepts in electro-and thermocatalysis toward hydrogen peroxide production, *J. Am. Chem. Soc.*, 2021, **143**(21), 7940–7957, DOI: 10.1021/jacs.0c13399.
107 S. Vijayaraghavan, H.-L. Yu, A. J. Senko, N. Rathi, A. M. Karim and D. W. Flaherty, to be submitted.

